Research Paper

Exploring aortic stiffness in aging mice: a comprehensive methodological overview

Laetitia Vanalderwiert[1,*], Auberi Henry[1,*], Juliana Martins de Souza E Silva[2], Daniel Carvajal-Berrio[3], Laurent Debelle[1], Amandine Wahart[1], Julia Marzi[3,5], Katja Schenke-Layland[3,5,6], Gilles Faury[7], Isabelle Six[8], Christian E.H. Schmelzer[2,4], Jürgen Brinckmann[10,11], Heiko Steenbock[10], Sébastien Almagro[1], Frédéric Delacoux[12], Stéphane Jaisson[1,9], Philippe Gillery[1,9], Pascal Maurice[1], Hervé Sartelet[1], Amar Bennasroune[1], Laurent Duca[1], Béatrice Romier[1], Sébastien Blaise[1]

[1]UMR CNRS 7369 MEDyC, University of Reims Champagne-Ardenne, Reims 51100, France
[2]Fraunhofer Institute for Microstructure of Materials and Systems IMWS, Halle (Saale) 06120, Germany
[3]Department for Medical Technologies and Regenerative Medicine, Institute of Biomedical Engineering, Eberhard Karls University Tübingen, Tübingen 72076, Germany
[4]Institute of Pharmacy, Faculty of Natural Sciences I, Martin Luther University Halle-Wittenberg, Halle (Saale) 06120, Germany
[5]NMI Natural and Medical Sciences Institute, Reutlingen 72770, Germany
[6]Department of Medicine/Cardiology, Cardiovascular Research Laboratories, David Geffen School of Medicine at UCLA, Los Angeles, CA 90095, USA
[7]INSERM, CHU Grenoble Alpes, University of Grenoble Alpes, Grenoble 38000, France
[8]Research Unit 7517, Pathophysiological Mechanisms and Consequences of Cardiovascular Calcifications (MP3CV), University of Picardie Jules Verne, Amiens, France
[9]Department of Biochemistry, Hospital of Reims, Reims, France
[10]Institute of Virology and Cell Biology, University of Lübeck, Lübeck, Germany
[11]Department of Dermatology, University of Lübeck, Lübeck, Germany
[12]International coordinator of The Exact and Natural Faculty of Reims, University of Reims Champagne-Ardenne, Reims 51100, France
[*]Equal contribution

Correspondence to: Sébastien Blaise; **email:** sebastien.blaise@univ-reims.fr
Keywords: aortic stiffness, extracellular matrix remodeling, elastic fibers, collagen fibers, ageing, methodological process
Received: December 28, 2023 **Accepted:** October 1, 2024 **Published:** December 2, 2024

ABSTRACT

Stiffening of the vascular network is associated with the early stages of vascular aging, leading to cardiovascular disorders (hypertension), renal failures, or neurodegenerative diseases (Alzheimer's). Unfortunately, many people remain undiagnosed because diagnostic methods are either unsuitable for a large population or unfamiliar to clinicians which favor the hypertension evaluation. In preclinical research, stiffness studies are often partially conducted. We think that the evaluation of aortic stiffness is essential as it would improve our understanding of aging diseases progression. We propose here a systematic method using decision trees in a multi-scale and multimodal approaches. Our method was evaluated by analyzing the aortic situation in old and young mice. We demonstrate that both the endothelial and smooth muscle cells exhibit pronounced functional alterations in favor of constriction. Additionally, there is significant remodeling of the extracellular matrix, leading to a drastic degradation of elastic fibers and the accumulation of collagen in the aortic wall. This series

of changes contributes to the development of vascular rigidity, a preliminary stage of arterial hypertension. Our results suggest that our method should improve preclinical understanding and encourage clinicians to equip themselves with tools assessing the vascular function, as it is an essential issue for preventing numerous pathologies.

INTRODUCTION

According to a recent study [1], adults aged 30 to 79 with arterial hypertension (AH) have increased from 650 million to 1.28 billion in 30 years. Nearly half of these individuals are unaware of their condition, primarily due to population growth, metabolic diseases (e.g., obesity, diabetes), and aging. AH significantly raises the risk of heart, brain, or kidney diseases, making it a leading global cause of mortality and morbidity [2]. Thus, adopting a total risk approach for early detection and effective management of AH could prevent cardiovascular complications.

Several studies [3, 4] suggest that the rise in blood pressure is only one symptom of an underlying cardiovascular disease and does not predict its course, except for severe AH. Systolic and diastolic pressures are important indicators but alone cannot reveal cellular or extracellular alterations in organs [5]. The duration of moderately high blood pressure values may play a role in organ functioning changes, making it essential to identify predictive parameters for cardiovascular risk. Some studies propose arterial stiffening measurement as a better parameter to predict risk and mortality in obese, diabetic, or aged patients [6–10].

Vascular stiffening results from vascular wall remodeling, including cellular and extracellular matrix (ECM) alterations [11]. The cellular compartment (vascular smooth muscle cells, SMC, and/or endothelial cells, EC) affects vasocontraction and vasodilation, while extracellular components like elastic and collagen fibers contribute to arterial mechanical properties. Collagen ensures vessel integrity and resistance to stretching [12], and elastic fibers provide flexibility and extensibility while allowing vessel retraction. With age, cellular composition and functionality change [13], and the ECM scaffold undergoes strong remodeling (elastic fiber degradation, collagen neo-synthesis).

To prevent cardiovascular issues, determining a patient's arterial age is crucial. In this context, the index of arterial stiffening may accurately estimate cardiovascular aging. Various methods are used, in hospitals or by medical practitioners, to measure arterial stiffness (i.e., magnetic resonance imaging (MRI), ultrasound). But others, requiring an invasive approach (i.e., atomic force microscopy (AFM), vascular reactivity), are for experimental research only. The method we present here was designed and tested to evaluate vascular ageing in a mouse model. Its accuracy relies on decision trees from both functional and anatomical perspectives.

RESULTS

A functional approach to study aortic stiffness

The assessment of aortic function and its level of stiffness can be easily conducted using general functional methods (e.g., ultrasound or measurement of arterial pressures) or more specific approaches at the cellular scale (i.e., EC and SMC) or the extracellular scale (elastic fibers) (Figure 1A). To illustrate this, we examined the cardiovascular function of young and old mice. Using high-frequency ultrasound, we obtained various anatomical and functional parameters of the heart and aorta. Cardiac parameters, including end-systolic and end-diastolic volumes, left ventricular mass, cardiac output, fractional area change, and fractional shortening, were significantly altered in the aged mice compared to the young mice, suggesting hypertrophy of the older heart (Table 1). Aged mice exhibited increased systolic and pulse pressures, as well as aortic pulse wave velocity (see Table 1). Ultrasound measurements of aortic anatomical parameters and estimations of local Young's modulus, compliance, and wall distensibility indicated arterial stiffness in aged mice (see Table 1). Muscle hypercontraction or ECM remodeling could explain the vascular stiffness observed. In comparison to young mice, aged mice displayed elevated production/expression of vasoconstrictor factors, such as tissue expression of α-SMA (smooth muscle actin), SM22a (smooth muscle), h-Caldesmon, and MLCK (Myosin light-chain kinase) (Figure 1B), as well as the expression and secretion of endothelin 1 (ET-1) in the plasma (Figure 1C, 1D).

By assessing vascular reactivity (Figure 1E), we examined the muscular status of the aorta and found that age limited the vasodilatory response to acetylcholine, while aortas from both groups responded similarly to phenylephrine stimulation. The reduced aortic relaxation mechanism could be attributed to decreased endothelial nitric oxide synthase (eNOS) gene expression (Figure 1C), with inducible nitric oxide synthase (iNOS) seemingly unaffected. The phosphorylation

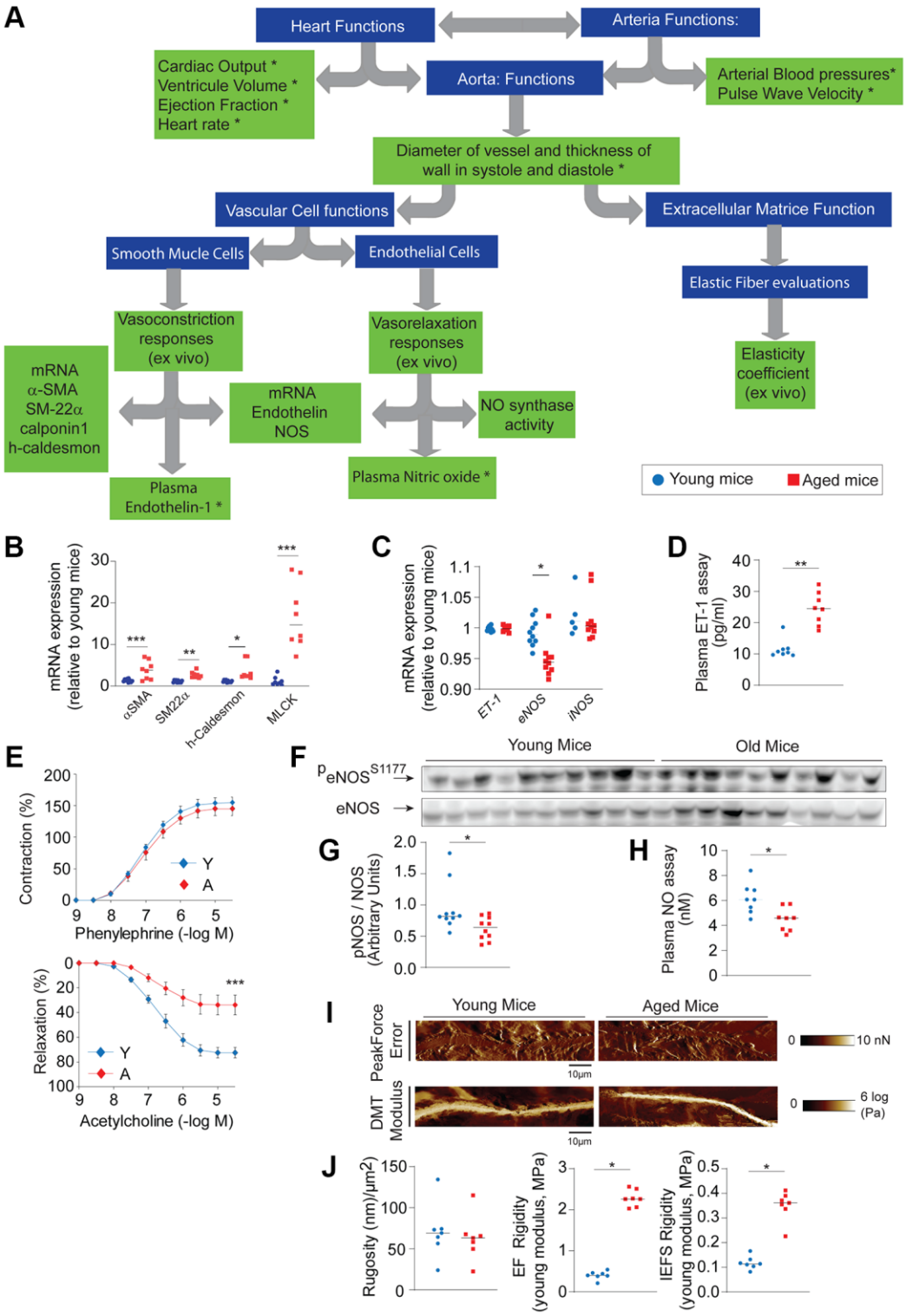

Figure 1. Functional evaluation of aortic stiffness between old (*n* = 5–10, red) and young (*n* = 5–10, blue) mice. (**A**) Decision tree allowing the functional evaluation of the animal with the elastic fiber. "*" identifies parameters that are methodologically accessible for clinical studies. (**B**) mRNA expression of vascular contraction markers (αSMA, Alpha Smooth Muscle Actin - SM22α, Smooth muscle protein 22-alpha - MLCK, Myosin light-chain kinase). (**C**) mRNA expression of endothelin (ET-1) and endothelial (eNOS) and inducible (iNOS) nitric oxide synthase. (**D**) Plasma assay of endothelin 1. (**E**) *Ex vivo* measurement of vascular reactivity after stimulation with phenylephrine or acetylcholine. (**F**, **G**) Western blot of native and phosphorylated forms of eNOS (panel **F**) and quantification of gray level by imageJ (panel **G**). (**H**) Plasma dosage of nitric oxide (NO). (**I**, **J**) Evaluation of extracellular matrix: by atomic force microscopy. (**I**) Imaging of elastic fibers (EF) with PeakForce error and DMT modulus (scale bar: 10 µm). (**J**) Quantifications of EF rugosity (left), stiffening of EF (middle) and inter-EF spaces (IEFS, right). Statistical test: Mann-Whitney. Mean+/− SEM. Significant differences ($^{*}p < 0.05$, $^{**}p < 0.001$, $^{***}p < 0.0001$, Mann-Whitney).

Table 1. Cardiovascular parameters obtained from young and aged mice.

		Young	Aged	Mann Whitney
		(*n* = 10)	(*n* = 10)	(*p*-value)
VASCULAR PARAMETERS	Systolic blood pressure (mmHg)	124.2 ± 0.8	139.5 ± 1.9	**0.0002**
	Diastolic blood pressure (mmHg)	48.3 ± 1.1	50.6 ± 1.5	0.1983
	Mean Arterial Pressure (mmHg)	73.6 ± 1.0	80.2 ± 1.6	**0.0011**
	Pulse Pressure (mmHg)	75.9 ± 0.3	88.9 ± 1.0	**0.0002**
	Pulse Wave Velocity (m/s)	0.2 ± 0.01	0.3 ± 0.02	**0.0015**
	Systole Diameter, *Ds* (mm)	1,68 ± 0.03	1.08 ± 0.05	**<0.0001**
	Diastole Diameter, *Dd* (mm)	1.48 ± 0.02	0.92 ± 0.04	**<0.0001**
	Systole Surface, As (mm^2)	2,21 ± 0.07	0.93 ± 0.08	**<0.0001**
	Diastole Surface (Ad, mm^2)	1,73 ± 0.06	0.69 ± 0.06	**<0.0001**
	Intima-media thickness (h, mm)	0.13 ± 0.003	0.14 ± 0.004	0.0972
	Local PWV (m/s)	0.87 ± 0.12	4.46 ± 0.75	**0.0013**
	Distensibility (*DC*, MPa^{-1})	203.6 ± 51.1	15.8 ± 7.5	**0.0108**
	Young modulus (E, MPa)	0.09 ± 0.02	1.72 ± 0.50	**0.0172**
	Local pulse pressure (DP, MPa)	0.002 ± 0.001	0.09 ± 0.03	**0.0127**
	Compliance (CC, mm^2/MPa)	142.3 ± 35.5	6.9 ± 3.3	**0.0085**
HEART PARAMETERS	Heart Rate in vigilante mice (bpm)	624.0 ± 9.8	632.3 ± 10.9	0.4053
	Heart Rate under anesthesia (bpm)	489.9 ± 16.2	417.4 ± 12.2	**0.0071**
	Flow rate aortic arch (mL/min)	22.97 ± 1.819	35.34 ± 3.546	**0.0057**
	Cardiac Output (mL/min)	12.92 ± 0.923	18.42 ± 1.099	**0.0172**
	Stroke Volume (µL)	32.71 ± 1.805	41.30 ± 1.988	0.0503
	Ejection Fraction (%)	50.64 ± 1.989	45.06 ± 2.362	0.1128
	Fraction Area Change (%)	47.08 ± 2.101	38.42 ± 3.723	**0.035**
	Fractional Shortening (%)	14.54 ± 2.094	21.89 ± 1.597	**0.033**
	Left ventricle end-diastolic volume (µL)	65.27 ± 2.186	75.87 ± 4.309	**0.0433**
	Left ventricle end-systolic volume (µL)	31.44 ± 1.005	39.51 ± 3.338	**0.0288**
	Left ventricle mass (mg)	99.09 ± 5.759	145.4 ± 8.825	**0.0039**

level of eNOS (Figure 1F, 1G) and plasma nitric oxide (NO) levels (Figure 1H) also decreased in the aorta of aged animals.

Beyond cells, the extracellular structures, such as elastic lamellae, are other components that could be affected. AFM (atomic force microscopy) results (Figure 1I, 1J) demonstrated an increase in the Young's modulus of elastic lamellae in young mice or in the interfiber spaces of aged aortas, consistent with stiffening of elastic fibers and possibly abnormal smooth muscle cell contraction.

General approaches to tissue structures

Alterations in each of the aortic layers (intima, media, adventitia), changes in cell composition (e.g., SMCs or ECs), and modifications in matrix structures (collagen or elastic fibers) contribute to the reduction in distensibility and/or vascular tone. The thickness of cell layers can be assessed through histological methods (e.g., hematoxylin-eosin - H&E) or immunohistochemistry staining, and by Raman imaging (Figure 2A).

In a morphological analysis of the aortic wall in old and young mice, H&E staining revealed a thicker intima-media and adventitia in old mice compared to young mice (Figure 2B). The increase in media thickness can be partly attributed to the accumulation of SMCs, as indicated by α-SMA immunostaining (Figure 2C, 2D). Discontinuities in the CD31 labeling suggest a loss of ECs in the intimal layer.

Raman spectroscopy, serving as a valuable alternative to histology and immunohistochemistry, excites the molecules within the aortic section under study and detects the diffusion of Raman photons generating a characteristic spectrum (Figure 2E, 2F). Furthermore, it allows for the reconstruction of images from all the

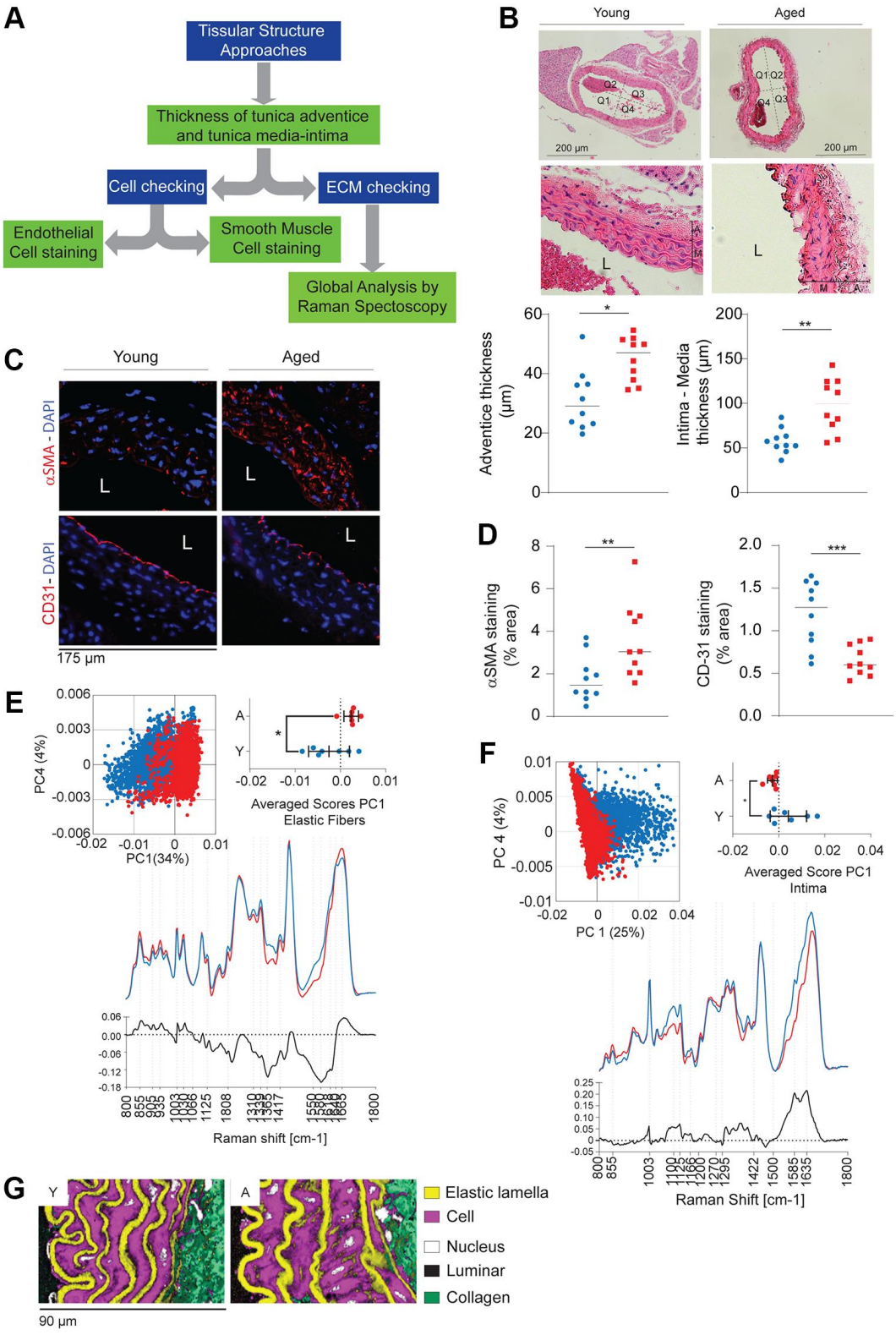

Figure 2. General evaluation of aortic wall remodeling between old (*n* = 5–10, red) and young (*n* = 5–10, blue) mice. (**A**) Decision tree allowing cellular and extracellular evaluation. (**B**) Histological staining (Hematoxylin-Oesin, HE) and quantification of the thickness of the tunica media and adventitia by ImageJ Software. (**C**) Immunohistology against αSMA (smooth muscle actin, specific marker for smooth muscle cells) and CD31 (specific marker for endothelial cells). DAPI (blue) identifies cell nuclei. (**D**) Quantification of CD31 and αSMA fluorescence (see Figure 2C) and related to DAPI fluorescence using ImageJ. (**E**, **F**) Examples of the spectra of the elastic fibers (**E**) and the tunica intima (**F**) obtained by Raman spectroscopy. (**G**) Reconstruction of the vascular wall from the spectra obtained previously (panels **E**, **F**). Statistical test: Mann-Whitney. Mean+/− SEM. Significant differences ($^{*}p < 0.05$, $^{**}p < 0.001$, $^{***}p < 0.0001$, Mann-Whitney).

collected spectra (Figure 2G). In the case of aging aortas, we observe an accumulation of cells (likely SMCs) in the media and thicker elastic lamellae, suggesting a significant alteration in the ECM.

Adventitia tunica analysis, focusing on collagen fibers

ECM remodeling in the adventitia primarily involves the deposition of collagen fibers, which offer protection to the aortic wall against overdistension during systolic cardiac phases. Any modification in this structure could either facilitate vessel rupture or, conversely, lead to increased wall rigidity. It's crucial to analyze the structures of collagen fibers, including assessing their quantity, types, and maturity levels (measured by crosslinking quantification) (Figure 3A). In aged mice, we observed an increase in collagen deposits, particularly type I fibrillar collagen, as indicated by mRNA expression (Figure 3B) and total collagen levels (Figure 3C) in the thoracic aorta. This increase was also confirmed by staining with picrosirius red (PSR) (Figure 3D).

Characterization of the maturation-degradation balance of collagen

The birefringence of collagens observed through polarized light microscopy of PSR-stained aorta slices also suggests an increase in type III collagen. The maturation of collagen fibers can be assessed by crosslinking quantification. In the aged thoracic aorta, compared to the young counterpart (Figure 3E), a significant increase is observed in the immature crosslinks, hydroxylysinonorleucine (HLNL), and histidinohydroxymerodesmosine (HHMD), while there's a decrease in the crosslink of mature hydroxylysine pyridinoline (HP). The immature dehydrohydroxy-lysinonorleucine (DHLNL) bond remains unchanged. Consequently, the sum of crosslinks (Total XL) increases in older abdominal aortas. The difference observed in the abdominal aorta is less pronounced than in the thoracic aorta (Supplementary Figure 1).

Characteristics of collagen degradation: Assessing the expression of enzymes involved in crosslink development, such as lysyl oxidase (LOX) and lysyl oxidase-like (LOXL-1 to -4), reveals that only LOXL1 and LOXL3 have increased expression in the aged aortas (Figure 3F). Lastly, the expression of collagenases (MMP1, MMP13, and MMP8) is significantly elevated in the old group compared to the young group (Figure 3G). The increase in collagen content and the number of crosslinks suggest that the adventitia layer may stiffen with age.

Intima-media analysis with a focus on elastic fibers

The ECM in the media layer of the aorta is mainly composed of lamellar units of concentric elastic fibers. A thorough examination of this intricate 3D scaffold requires high-resolution microscopy techniques such as scanning electron microscopy (SEM) and 3D X-ray computed tomography (X-ray CT) (Figure 4A). SEM reveals alterations in elastic fibers in aged mice, where the fibers are less distinct compared to those in young aortas (Figure 4B). This disorganization is also visible through X-ray CT (Figure 4C). Simple image segmentation using a grayscale threshold allows for the separation of media cells (pseudo-stained in green) from the elastic lamellae (pseudo-stained in orange) in the young mouse specimen. In the imaged area, the elastic fiber network in the old mouse aorta appears to have a less ordered structure (Figure 4C). Comparing the high-resolution X-ray image of the aorta in an older animal to a younger one, a clear distinction in elastin organization is evident, characterized by a decrease in the quantity and thickness of lamellae, as shown in Figure 4C.

Characterization of the elastogenesis

The observed changes in the elastic fiber scaffold in the aged mouse specimen are likely due to elastolysis processes, including elastin fragmentation, elastin peptide production, and elastase activities. Nevertheless, elastogenesis and elastosis should not be overlooked (Figure 5A). Elastogenesis is characterized by the expression of elastin (ELN) and microfibrillar glyco-proteins, such as fibrillins (e.g., FBN1), fibulins (e.g., FBLN5), or latent transforming growth factor-beta binding proteins (e.g., LTBP4), and the formation of crosslink patterns that indicate fiber maturity.

When comparing aged and young mouse aortas, the expression of mRNAs for ELN, FBLN-5, and LTBP4 is identical in both groups studied (Figure 5B). Only the mRNA expression of FBN-1 is significantly increased. Furthermore, the total insoluble elastin decreases, suggesting a loss of integrity of this protein (Figure 5C). When evaluated individually, no significant difference is observed in crosslinks within the thoracic (or abdominal) aorta of the two groups (Figure 5D and Supplementary Figure 1). However, the sum of all different crosslinking patterns (Total XL) significantly decreases in aged aortas compared to young aortas, confirming the disorganization of these fibers.

Characterization of the elastolysis

In addition to assessing elastogenesis, understanding elastolysis is a crucial aspect for determining the degree of vascular stiffness (Figure 5A). Histological methods such as Hart's staining or elastin autofluorescence enable an estimation of the integrity of elastic fibers by measuring their thickness or identifying ruptures. To facilitate measurements, the vessel is divided into four

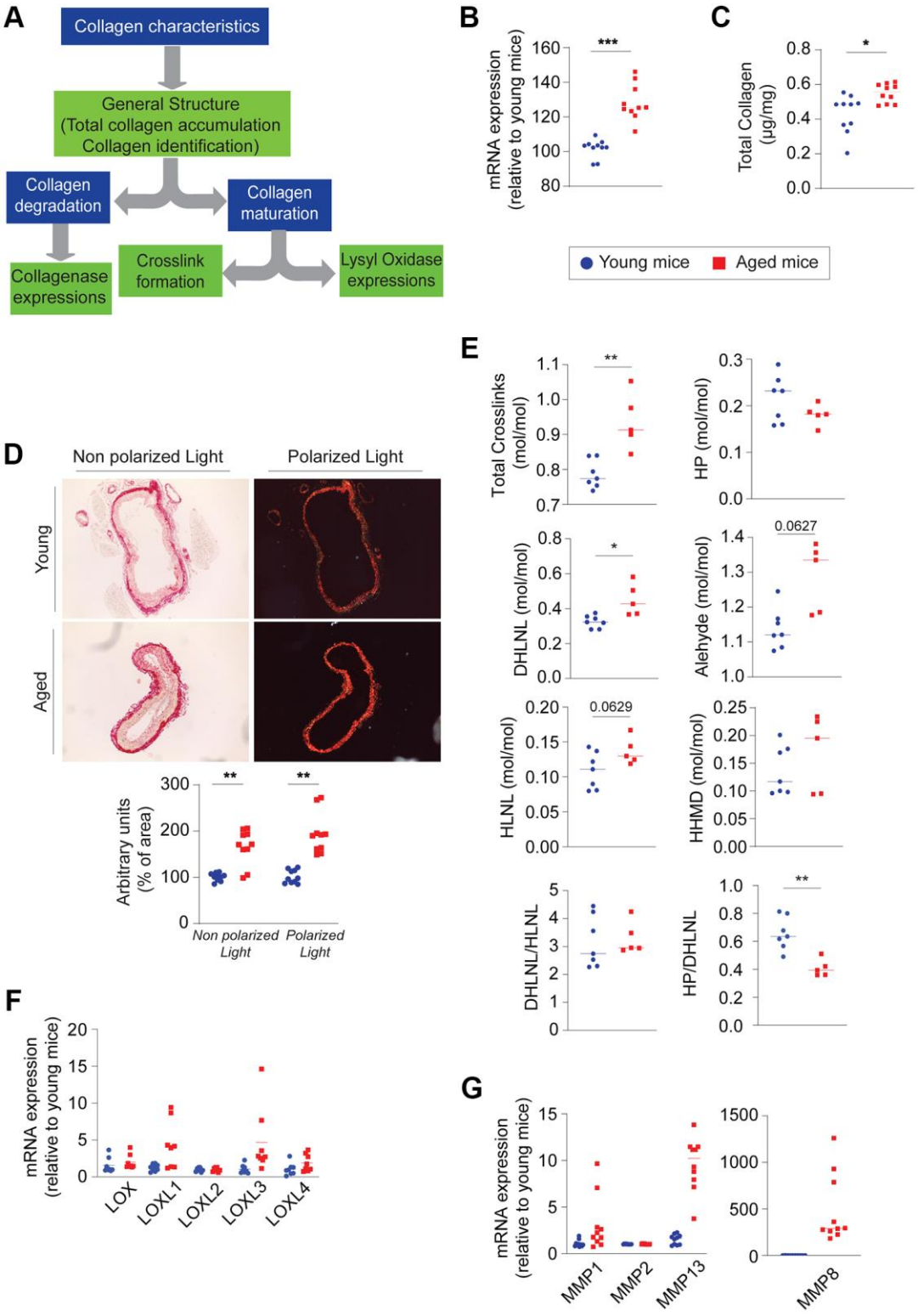

Figure 3. Evaluation of the collagen component within the aging aortic wall (*n* = 5–10, red) and young (*n* = 5–10, blue). (**A**) Decision tree allowing the evaluation of collagen. (**B**) mRNA expression of collagen (1a) type I. (**C**) Quantification of total collagen on the whole aorta. (**D**) Histological staining with picrosirius red and visualization in polarized or non-polarized light (left panel). Quantification of colorized collagen as a function of image area using ImageJ Software (right panel). (**E**) Quantification of the different crosslinks formed within collagen fibers such as hydroxylysyl pyridinoline (HP), hydroxylysinonorleucine (HLNL), dihydroxylysinonorleucine (DHLNL), histidinohydroxymerodesmosine (HHMD) in the thoracic aorta. (**F**) mRNA expression of lysyl-oxidase (LOX) and lysyl-oxidase like 1 to 4 (LOXL1, −2, −3, −4). (**G**) mRNA expression of metalloproteinases 1, 2, 13 and 8 (MMP1, −2, 13, −8). Statistical test: Mann-Whitney. Mean +/− SEM. Significant differences ($^{*}p < 0.05$, $^{**}p < 0.001$, $^{***}p < 0.0001$, Mann-Whitney).

quadrants (Figure 5E). The total number of elastic fiber ruptures is higher in old aortas compared to young aortas (Figure 5F). Examining individual fibers, we observe these ruptures across all six concentric lamellae without distinction (Figure 5G). Elastic fiber fragmentation can also be determined by measuring the quantity of elastin-derived peptides (EDP) or desmosines found in the plasma, which are significantly increased in aged mice (Figure 5H).

Another approach to detect increased elastolysis within aged aortas is quantifying the expression of elastases such as MMP2, MMP9, neutrophil elastase, and cathepsin S (Figure 5I), or the activity of cathepsin S in plasma (Figure 5J). However, these increased activities can be counterbalanced by the presence of their natural inhibitors. In older mice, inhibitors of MMP9, neutrophil elastase, or cathepsin S (e.g., TIMP1 (tissue inhibitor of metalloproteinase), SERPIN

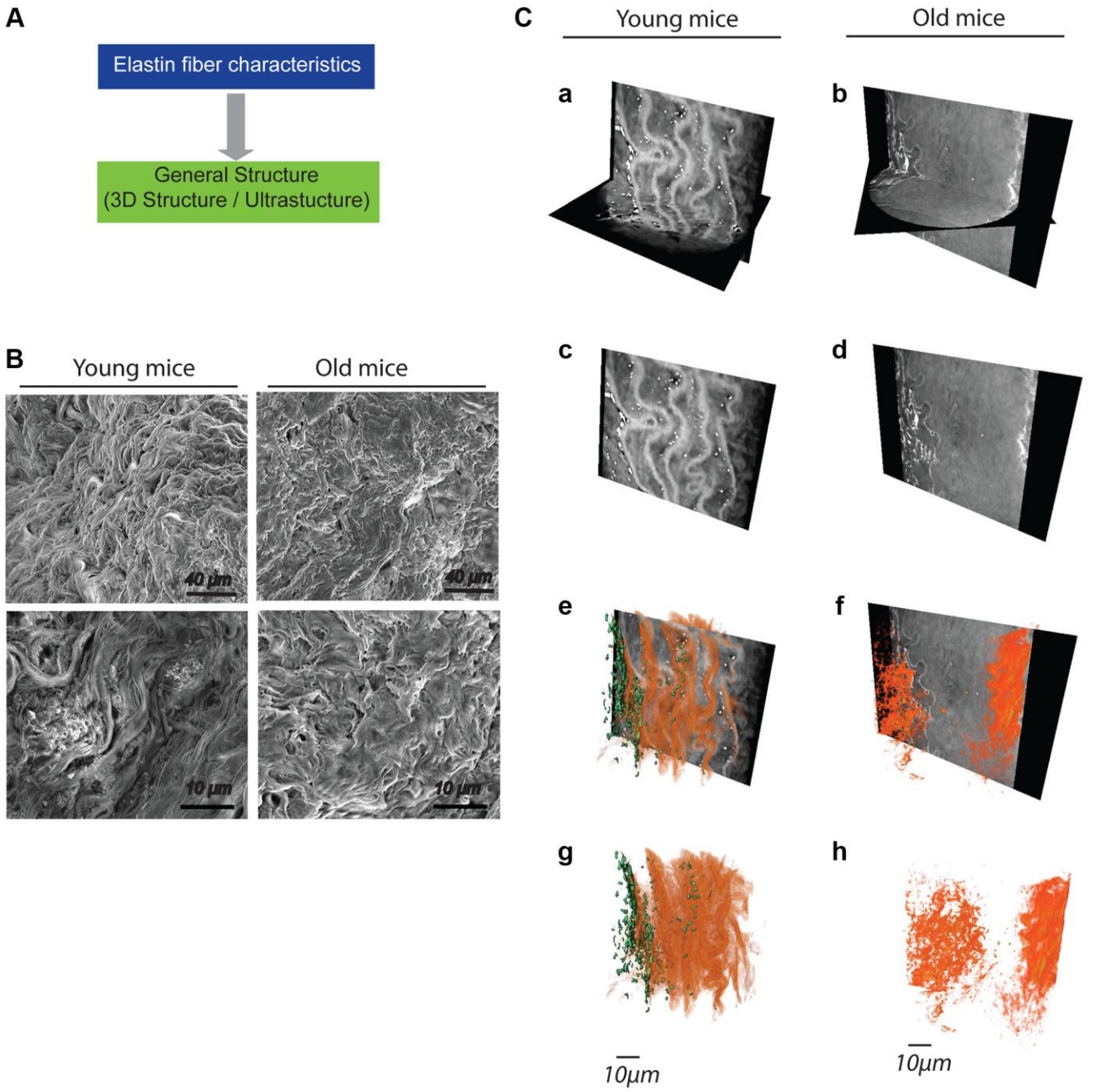

Figure 4. General impact of aging on the general structuring of elastic fibers within the aortas (*n* = 4/group). (**A**) Decision tree allowing the evaluation of the general organization of elastic fibers. (**B**) Low (top panels) and high (bottom panels) magnification images obtained from scanning electron microscopy. (**C**) Images obtained by high-resolution X-ray microscopy (panels **a**–**f**). A 3D reconstruction of the network of elastic fibers (red) and cells (green) is made from the images (panels **e**–**h**).

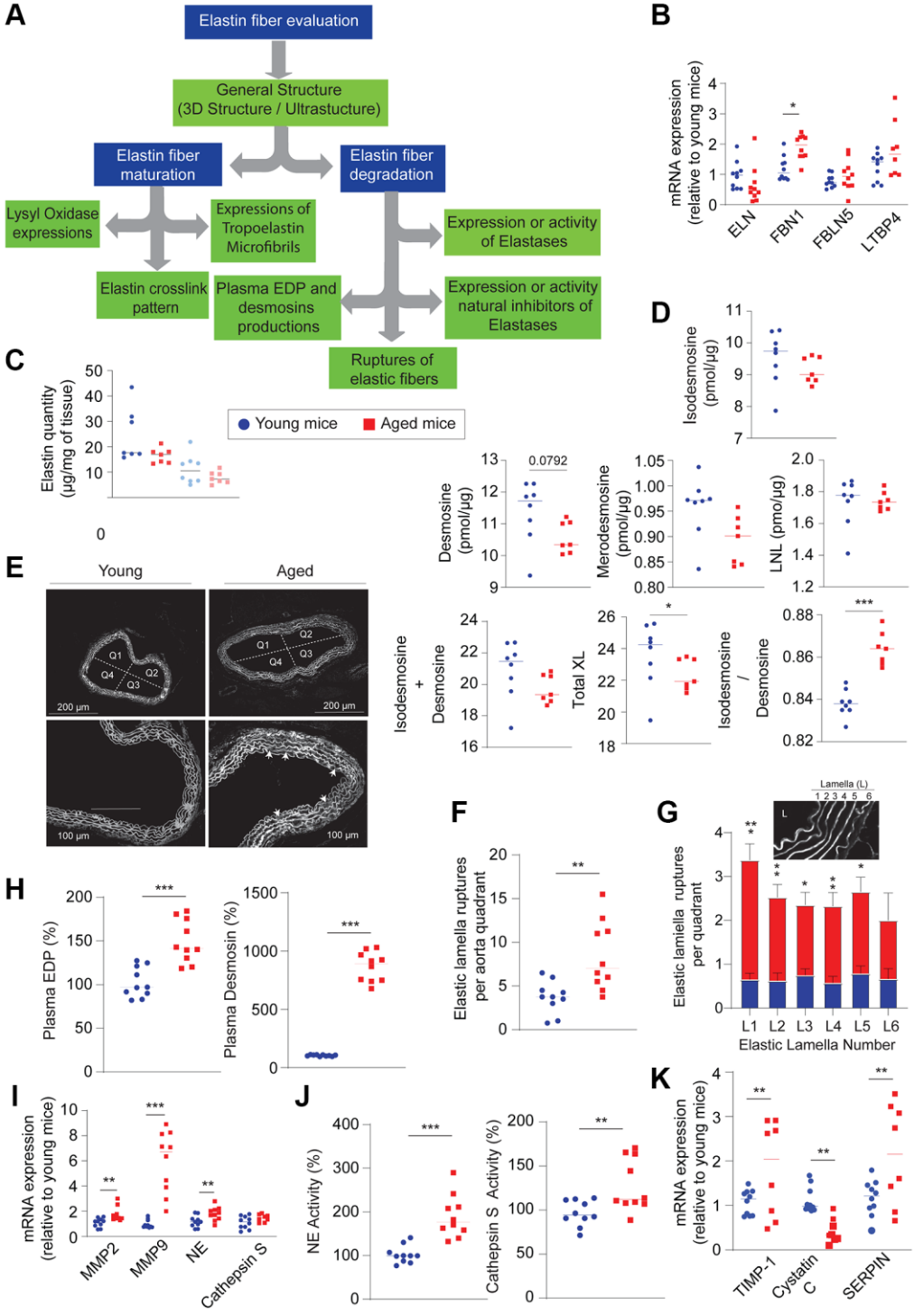

Figure 5. Evaluation of elastic fibers within the aortic wall (*n* = 5–10, red) and young (*n* = 5–10, blue). (**A**) Decision tree allowing the evaluation of elastogenesis and elastolysis. (**B**) mRNA expression of elastin (ELN), fibulin 5 (FBLN5), fibrillin 1 (FBN1), latent transforming growth factor beta binding protein 4 (LTBP4). (**C**) Quantification of total elastin on the thoracic aorta (dark blue circle and dark red square) and the abdominal aorta (light blue circle and light red square). (**D**) Quantification of the different crosslinks formed within elastic fibers such as isodesmosine, desmosine, merodesmosine, lysinonorleucine (LNL) in the thoracic aorta. (**E**) Visualization of the ruptures (arrowheads) of the elastic lamellae observed by the autofluorescence of elastin. (**F**) Total quantification of the ruptures observed in Figure 5E. (**G**) Counting the number of ruptures observed for each elastic lamella and determining from Figure E. (**H**) Plasma quantification of elastin-derived peptides (EDP) and desmosines. (**I**) mRNA expression of elastases such as matrix metalloproteinase 2 and 9 (MMP2 and MMP9), neutrophil elastase (NE) and cathepsin S. (**J**) Plasma activities of neutrophil elastase (NE) and cathepsin S. (**K**) mRNA expression of natural elastase inhibitors, TIMP1 (tissue inhibitor of metalloproteinase), cystatin C, Serine protein inhibitor (SERPIN). Statistical test: Mann-Whitney. Mean +/− SEM. Significant differences ($^{*}p < 0.05$, $^{**}p < 0.001$, $^{***}p < 0.0001$, Mann-Whitney).

(Serine protein inhibitor), cystatin C, respectively) have significantly increased expression (Figure 5K), suggesting a mitigation of the effects of proteases.

DISCUSSION

Among the critical factors contributing to vascular aging, the deformability of elastic arteries, as determined by elastance-compliance, plays a significant role, possibly on par with or even surpassing the impact of hypertension [13, 14]. In this study, we have, for the first time, amalgamated classical and innovative methods into a single framework for assessing vascular stiffness, considering both cellular and extracellular parameters that may influence it. We have given precedence to methodologies both in terms of function and anatomy (see Figure 1A and Supplementary Figure 2) to streamline future research, be it fundamental, clinical, or diagnostic, in the field of vascular stiffness.

The points we address in these decision trees allow for a comprehensive characterization of vascular stiffness for preclinical studies. It is important to identify the cellular component (i.e., endothelial and smooth muscle cells), as numerous studies have already illustrated. In these same studies, the contribution of extracellular matrix remodeling is generally not mentioned. This could be due to the authors' lack of knowledge and/or experience in ECM analysis.

However, whether for preclinical or clinical studies, it is crucial to identify the reasons for vascular stiffness — cells or ECM— as therapeutic approaches can be very different.

In clinical conditions, few parameters are currently available using non-invasive imaging methods, such as PWV and aortic elasticity (Figure 1A and Supplementary Table 1). Plasma biomarkers can also be evaluated: levels of NO, endothelin, elastase activity, or soluble elastin fragments (Supplementary Figure 2 and Supplementary Table 1).

Although the structures of mouse and human aortas are quite different, the aging process between young and old mice compared to humans is remarkably comparable (Supplementary Table 1). This comparison underscores the relevance of our methods across species. To illustrate the practicality of this methodological approach, we applied our decision trees to a study comparing aortic stiffness in old and young mice (without apparent pathology).

In our proposed decision trees, the primary factor under scrutiny by clinicians and basic researchers is the functional alteration of SMCs and/or ECs. These disruptions often lead to increased SMC contraction due to elevated levels of plasma vasoconstrictor agents, such as endothelin 1, and a reduction in pro-relaxing factors like nitric oxide production. Furthermore, SMC hyperproliferation intensifies vasoconstriction. When evaluating vascular stiffness and its impact on systolic pressure, the remodeling of cellular components, including SMCs and ECs, should not be overlooked. It is important to note that functional measurements, except for blood pressure, were performed in anesthetized mice. Anesthesia can undoubtedly minimize the differences between groups, here elderly vs. young individuals. The application of these methods in awake individuals, as in humans, would undoubtedly be more relevant. Indeed, these functional measurements can be performed on awake patients, either in specialized medical imaging facilities or by a general practitioner trained in ultrasound and pulse wave velocity measurement.

Although the cellular component significantly contributes to vascular resistance, the fundamental elements of the ECM (elastic and collagen fibers) play a crucial role in maintaining aortic structural and functional integrity. Therefore, during systolic phases, collagen fibers bear more than half of the mechanical load on the vessel, serving to safeguard the aortic wall from overdistension. When collagen synthesis is downregulated or when structural alterations occur, the vessel wall becomes more susceptible to fatigue and failure, increasing the likelihood of multiple arterial ruptures and aortic dissections [15, 16]. On the contrary, an excess of these fibers or excessive cross-linking between them has been associated with elevated arterial pressures and vascular stiffening [17–19].

In addition to these structural components, the inflammatory state of the arterial wall also plays a critical role in vascular aging. Chronic, low-grade inflammation is a common feature of aging tissues and contributes significantly to vascular dysfunction. During aging, low-grade inflammation is consistently observed in many tissues. This is particularly evident in the arterial component, where immune cell infiltration is noted. Such inflammation, which could be quantified by flow cytometry, can lead to cellular dysfunction by disrupting molecular processes like autophagy, proliferation, differentiation, and cellular calcification. Additionally, the presence of leukocytes can release proteases (such as neutrophil elastase, cathepsin S, and MMPs), contributing to the degradation of both collagen and elastic fibers. The degradation of these fibers due to inflammatory processes further complicates the structural integrity of the aorta. This interaction between inflammation and ECM remodeling underscores the need for comprehensive visualization techniques to assess fiber integrity.

Collagen visualization can be accomplished using various classic, rapid, and cost-effective histological methods, such as Masson's trichrome and picrosirius red (PSR). Unlike Masson's trichrome, PSR allows for the visualization of both collagen fiber types I and III [20]. When observed under polarized light microscopy, PSR-stained samples exhibit type I collagen fibers (thicker fibers) with yellow-orange birefringence and type III collagen (thinner fibers) with green birefringence. However, it's worth noting that some studies have contested this differentiation. In our study, we have adopted a comprehensive quantification approach that encompasses both type I and type III collagen fibers.

Alternatively, a more costly solution involves multi-photon microscopy with second harmonic generation (SHG), where the primary source of the signal is fibrillar collagen (type I). This technique allows for the identification of the macromolecular organization of fibrillar collagen (type I) exclusively, and it permits the application of specific immunostaining for other collagen types. Significantly increased expression of aortic collagen types I and III, during aging, may result in impaired fibril formation and, consequently, decreased tensile strength of vascular tissue [21, 22]. These increases, particularly in type III collagen, could be a warning sign of a risk of dissection and aneurysm.

While the accumulation of collagen fibers affects the radius-tension relationship (Laplace's law), the elastic lamellae confer elastance and compliance properties to blood vessels. Several methods are available to study the degree of elasticity (or stiffening) in elastic fibers. Ultrasound and MRI approaches allow us to determine the degree of aorta stiffening by measuring Young's modulus, compliance, or pulse-wave velocity. These techniques are readily accessible in healthcare institutions, making it reasonable to consider them for diagnosing vascular rigidity. We directly determined the Young's modulus of elastic fibers, as described by Berquant et al. [23]. Young's modulus measurements obtained through ultrasound approaches (*in vivo*) or AFM (*in vitro*) reveal a significant stiffening of elastic fibers in aged aortas compared to those in young mice, suggesting a modification in the integrity of these elastic fibers.

Elastic lamellae, or elastic fibers, possess a complex structure comprising numerous proteins. The most abundant among these is a large biopolymer known as elastin, which is stabilized by microfibrils and covalent cross-links. These microfibrils include fibrillins, fibulins, and latent transforming growth factor-β binding proteins (LTBPs). Simultaneously, cross-linking enzymes such as lysyl oxidase (LOX) and lysyl oxidase-like 1 facilitate intra-fiber crosslinks, including desmosine, isodesmosine, or merodesmosine, markers of elastic fibers maturity. Current methods for identifying the development of the scaffold forming the elastic fiber are mostly limited to mRNA or protein expression, providing information only regarding the presence or absence of elastin and microfibrils. In contrast, biochemical analysis of crosslinks offers insight into fiber maturity.

Combining various imaging methods such as Raman spectroscopy, three-dimensional X-ray imaging, and scanning electron microscopy can complement biochemical approaches. Images obtained by high-resolution X-ray imaging (Figure 4C) show a morphological change likely due to lamellae rupture in old animals. The visualization of lamellae differs between SEM and X-ray imaging, with SEM capturing surface details while high-resolution X-ray imaging provides insight into the internal structure. This discrepancy highlights the value of using multiple microscopic methods to understand elastin distribution in biological samples. Raman spectroscopy and X-ray tomography do not require molecular labeling or contrast agents and yield high-resolution quantitative images of the spatial distribution of ECM constituents in biological tissue sections (paraffin or frozen), living tissue, or even *in vivo* (e.g., fiber optics coupled with Raman spectroscopy) [24]. This minimally invasive method, although still experimental, holds potential for aiding in the pathological diagnosis of ECM [25]. In the absence of techniques like Raman spectroscopy, standard histological methods (e.g., Weigert's, van Gieson's, Hart's staining) [11], or elastin autofluorescence [20], provide information about the general appearance of the fibers (thickness, quantity) and are user-friendly.

Several studies, including our own, reveal that three-dimensional X-ray imaging and scanning electron microscopy are currently the only approaches that offer high-resolution images to visualize ruptures and defects in the fiber architecture of the intima-media tunica. Fractures can be identified [26, 27], as well as the interaction of the elastic laminae with other surrounding tissues (e.g., perivascular adipose tissue) [28, 29]. However, these methods cannot provide information about the elastic properties of the fibers during systole or diastole, necessitating simulations of these cardiovascular phases by pressurizing the vessel upstream of the imagery [30].

Nonetheless, these imaging methods are primarily limited to providing morphological information and lack the resolution to detect local molecular events on elastic fibers or collagen, such as post-translational modifications (e.g., glycation, carbamylation, N-homocysteinylation, glycosylation, etc.) or crosslinks between elastin fibers (desmosine, isodesmosine),

indicative of fiber aging [31, 32]. Expression levels (mRNA or proteins) and cross-links can be measured relatively easily [20, 33, 34]. In our study involving old mice, we observe that collagen cross-links are favored, while those of elastic fibers are reduced compared to young mice. This suggests a loss of structural integrity in elastic fibers in favor of collagen fibers, contributing to vessel stiffening. These alterations in elastic fibers, including fragmentations evident through elastin autofluorescence or reduced cross-link quantities, can be detected through measurements of desmosines and/or elastin-derived peptides (soluble fraction of elastin) in plasma [20, 35]. These markers correlate with aging [36, 37]. In keeping with Paczek et al., we demonstrate that the synthesis and plasma activity of proteases (e.g., cathepsin S, neutrophil elastase) increase with age, potentially explaining age-related diseases and arterial stiffening [38, 39]. Consequently, these plasma assays, including these protease activities or elastin fragments degraded (EDP and/or desmosines), could easily be performed by medical analytical laboratories. Those plasma data coupled with functional imagery (MRI or ultrasound) could integrate into clinical diagnostic methods and provide the general practitioner or specialist with major information for diagnosing arterial stiffening. Then, the complications of vascular stiffness could be anticipated and a therapeutic strategy adapted, such as an anti-hypertensive treatment, for example.

As a proof of concept for future studies in humans, it would be interesting to use our functional and anatomical decision trees to provide a risk score that could predict the occurrence of future arterial stiffness and hypertension. This risk score should take into account functional data such as pulse wave velocity (>10 m/s) and/or Young's modulus ($<1.8 \times 10^3$ kPa) of the aorta obtained by ultrasound or MRI [40, 41]. Additionally, this score would be augmented by plasma factors such as endothelial markers (NO, <22 mM and ET-1, >2.02 pg/mL) [42, 43] and factors involved in elastolysis, such as plasma activities of elastases (NE, >243.9 ng/mL and cathepsin S, >26.28 ng/mL) [44, 45], as well as markers of elastic fiber degradation (i.e., elastin-derived peptides (EDP, >4.9 ng/mL and/or plasma desmosines, >0.4 ng/mL) [46–48]. The resulting score could allow clinicians to anticipate the implementation of antihypertensive treatments, for example. Moreover, all these data could eventually be integrated into other cardiovascular risk scores, such as the Framingham Risk Score. This score predicts various aspects of cardiovascular disease risk by integrating the age and gender of the patient, their systolic blood pressure, total plasma cholesterol levels, HDL, and CRP. It also considers whether patients are diabetic, smokers, and the treatments they use. But this Framingham Risk Score, as a lot of other cardiovascular scoring systems, can explain no more than 50% of the overall risk of developing cardiovascular disease [49–52]. Improving the robustness of these scores could involve integrating parameters describing vascular stiffness in our study into the calculation method.

The study concludes by emphasizing the need for a multimodal and multi-level approach to study arterial stiffening, providing valuable insights for diagnosis and preclinical research into molecular mechanisms. Detecting and preventing aortic stiffness is deemed crucial in clinical practice and fundamental research, suggesting the integration of new diagnostic options into routine medical practices. However, the article acknowledges the current applicability of non-invasive imaging approaches primarily in preclinical research and calls for the development of low-cost, easy, and rapid protocols for clinical use.

MATERIALS AND METHODS

Animal models

All mouse procedures conformed to the Guide for Care and Use of Laboratory Animals of the US National Institutes of Health and were approved by the Animal Subjects Committee of Champagne-Ardenne (2018032113171684v8-15413). C57BL/6N mice (6 and 20 months old) were purchased from Janvier (Le Genest-Saint-Isle, France) and housed in a 12:12-hour light/dark cycle, temperature- and humidity-controlled environment. They had ad libitum access to a standard diet (AIN-93 M rodent diet, Special Diet Service, UK), and water during the experimental period.

Functional parameters

Measurement of blood pressure

The study employs the non-invasive tail-cuff method to measure blood pressure in animals, avoiding anesthesia or surgery. Adaptation and handling are required, with regular daily sessions. Parameters include pulse, systolic and diastolic pressures, from which mean arterial pressure and pulse pressure are derived. Hypertension is determined based on statistical differences in pressure between aged and young mice.

Pulse wave velocity (PWV)

Velocity measurements are conducted in anesthetized animals (4% isoflurane, 10 min). The measurement can be performed using ultrasound probes (Indus Instruments, Webster, TX, USA), with one probe placed at the level of the aortic arch and the other at the level of the abdominal thoracic aorta near the bifurcation of the iliac arteries. While Doppler ultrasound systems can measure velocity limited to specific portions of arteries

(such as carotids and the aortic arch), this method considers the entire aorta, providing a more comprehensive assessment of vessel rigidity.

High-frequency ultrasound imaging

Under isoflurane anesthesia, we measured heart parameters. The Vevo3000 system assessed left ventricle functions, aortic arch dimensions, pulse wave velocity, and intima-media thickness. Distensibility factor (D) and Young's modulus (E) were derived using relevant equations such as: the Bramwell and Hill equation [53] and the Moens-Korteweg equation. Pressure variation and compliance were deduced following Brands' methodology [54].

Vascular reactivity

We investigated the effects of aging on *ex vivo* aortic reactivity. Wild-type mice were anesthetized by intraperitoneal injections of pentobarbital sodium (150 mg/kg). Once euthanasia was complete, their hearts were removed. Vascular reactivity studies were carried out, as described in [55].

Biochemical parameters

Plasma assay

Peripheral blood from mice was collected in heparinized tubes by retroorbital puncture, and the plasma was stored at −80°C. Evaluations of elastin-derived peptide concentrations were performed using a commercially available kit (Biocolor, Antrim, UK) according to [56] and a desmosine ELISA kit (Cusabio Technology LLC, Houston, TX, USA) according to [20]. A neutrophil elastase activity assay and a cathepsin activity assay (Abcam, Cambridge, UK) were used to measure neutrophil elastase and cathepsin S activities, respectively [20]. Endothelin1 was quantified with an ELISA kit (Mybiosource, Vancouver, Canada).

Total collagen and elastin quantifications

Tissue was digested with HCl and its collagen content was determined from collagen assay kit (Sigma-Aldrich, St. Louis, MO, USA). Quantification of total elastin was carried out according to the protocol described in the study by Nave et al. [57].

Cross-linking assay

Protein analysis followed the protocol described [57]. Collagen crosslink analysis involved sodium borohydride reduction, bacterial collagenase digestion, and HCl hydrolysis. Crosslinked soluble fractions were hydrolyzed and precleared, with eluates analyzed on an amino acid analyzer. Crosslink nomenclature denotes reduced variants. Collagen content, based on hydroxyproline, was calculated from hydrolyzed collagenase-soluble samples. For protein and elastin crosslinks, samples underwent collagenase digestion. Soluble collagen underwent hydrolysis, while the residual fraction was alkali-extracted. Elastin and non-collagenous proteins in the supernatant were hydrolyzed. Elastin crosslinks in the NaOH-insoluble fraction were analyzed after CF-11 preclearance. The study's approach provides insights into collagen, protein, and elastin crosslinks.

Gene expression

The analysis utilized qPCR, with RNA extraction, cDNA synthesis, and real-time PCR as previously described [20]. The housekeeping genes 36B4 and RPS26 normalized RNA expression, calculated using the $2^{-\Delta\Delta CT}$ method. Detailed primer sequences are available in Supplementary Table 2. The study's comprehensive approach provides insights into collagen, protein, elastin crosslinks, and gene expression.

Western blotting

Western blotting was performed as previously described by Blaise et al. [56]. The antibodies, including endothelial nitric oxide synthase (eNOS, 32027S, dilution 1/1000) and its phosphorylated form (p-NOS, 9570S, dilution 1/1000), were purchased from Cell Signaling Technology (Danvers, MA, USA).

Imaging parameters

Histology approaches

From paraffin cross-sections (5 µm thickness) of aortas, deparaffinization and rehydration were performed before staining with Hematoxylin-Eosin (H&E) or red picrosirius, as described [20]. Autofluorescence of elastin at a wavelength of 488 nm was observed from the H&E staining. Thickness measurements of intima-media and adventitia tunica were conducted using the ImageJ Software.

Raman spectroscopy/imaging

Raman measurements used a Witec alpha 300R confocal Raman microscope on deparaffinized aorta cross-sections. Samples were kept hydrated, and underwent imaging with a green laser (532 nm). Two images per sample were acquired, each covering an 80 × 90 µm area at 0.5 × 0.5 µm/pixel resolution. Data preprocessing included cosmic ray removal, baseline correction, cropping, and normalization. True component analysis (TCA) generated intensity distribution heatmaps, identifying prevalent spectral signatures. Principal component analysis (PCA) on single spectra extracted from TCA images allowed in-depth molecular analysis. PCA was applied separately for elastic fibers and interfibrillar ECM.

Atomic force microscopy (AFM)

Frozen 10 µm-thick aorta cross-sections were incubated in KH solution for equilibration at 37°C. The prepared

samples were placed onto the microscope stage and observed with bright field illumination to locate the spots of interest. Analysis was performed using AFM as described [23, 58]. Analyses were performed at three different locations in each cross-section, for a total of nine cross-sections obtained from three different mice.

High-resolution X-ray microscopy

Aorta underwent paraffin removal and staining before manual sectioning. Sections were affixed to metallic pins for X-ray imaging using a Carl Zeiss Xradia 810 Ultra microscope with a chromium source. Zernike phase-contrast and a field-of-view of 64 µm² were employed for imaging. A total of 901 projection images were acquired during a 180-degree sample rotation. Reconstruction, using a filtered back-projection algorithm, resulted in isotropic voxel-sized (128 nm) volumetric images. Stitching of images was performed, and tomograms were exported for visualization in Thermo Fischer Avizo software. This methodology provided detailed X-ray images for comparative analysis of aortic structures in young and old mice.

Scanning electron microscopy

Defrosted samples were deposited onto a SEM stub and treated with NanoSuit® Aqueous Solution (Electron Microscopy Sciences) according to the manufacturer's instructions. Samples were imaged in a Scanning Electron Microscope FEI Quanta 3D FEG Dual-Beam working at an acceleration voltage of 5 kV.

Statistical analyses

Data were prospectively collected and analyzed using StatView 5 software for Windows (SAS Institute, Berkley, CA, USA). In agreement with random sampling analyses, comparisons between groups are presented as mean ± SEM. Nonparametric statistics (Mann-Whitney *U*-test) were used. For all analyses, a p-value < 0.05 was considered to indicate statistical significance.

Availability of data and materials

The authors declare that all supporting data are available within the article and its Supplementary Materials. The corresponding authors may provide additional data supporting the findings of this study upon reasonable request.

AUTHOR CONTRIBUTIONS

The conception and design of the study - AH, LV, JM, KSL, JMSS, CHES, JB, IS, BR, SB. The acquisition of data - AH, LV, AW, DACB, JB, JM, JMSS, CHES, IS, BR, SB. Analysis and interpretation of data - AH, LV, AW, DACB, JB, HSt, JM, KSL, JMSS, CHES, IS, HSa. Drafting the article - AH, LV, KSL, IS, GF, SJ, PG, JB, CHES, LDe, SA, PM, AB, LM, LDu, FD, BR, SB. Critical revision - AH, LV, KSL, IS, GF, SJ, PG, JB, CHES, SA, LDe, VD, PM, AB, LM, LDu, FD, BR, SB. All co-authors approved the final version.

ACKNOWLEDGMENTS

We wish to thank Dr. Christian Garbar (Godinot Institute, Reims, France) for excellent help in histology, and Cathy Hachet and Olivier Bocquet (University of Reims Champagne-Ardenne, Reims, France) and Elaine Davis and Ling Li (McGill University, Montreal, Canada) for technical help. We thank Dr. Alexandre Berquant and Jean-Luc Breda for their work associated to PICT ("Imagerie Cellulaire et Tissulaire") and URCAnim facilities, respectively.

CONFLICTS OF INTEREST

The authors declare no conflicts of interest related to this study.

ETHICAL STATEMENT

All animal experiments were approved by the Animal Subjects Committee of Champagne-Ardenne (Permission No. 2018032113171684v8-15413) and conformed to the Guide for Care and Use of Laboratory Animals of the US National Institutes of Health.

FUNDING

This work was supported by funding from the CNRS, the University of Reims Champagne-Ardenne, Région Grand-Est (OMAGE program, France), University Hospital Federations (Entitled assessment and integrative research on. remodeling-inflammation-metabolic stress in systemic and hepatogastrointestinal metabolic diseases, FHU-ARRIMAGE) and European funds FEDER. AW was supported by research grants from the Région Champagne-Ardenne. LV was supported by research grants from URCA and CEHS was supported by Fraunhofer Internal Programs under Grant No. Attract 069-608203.

REFERENCES

1. NCD Risk Factor Collaboration (NCD-RisC). Worldwide trends in hypertension prevalence and progress in treatment and control from 1990 to 2019: a pooled analysis of 1201 population-representative studies with 104 million participants. Lancet. 2021; 398:957–80. https://doi.org/10.1016/S0140-6736(21)01330-1 PMID:34450083

2. Zhang Y, Lacolley P, Protogerou AD, Safar ME. Arterial Stiffness in Hypertension and Function of Large Arteries. Am J Hypertens. 2020; 33:291–6. https://doi.org/10.1093/ajh/hpz193 PMID:32060496

3. Boutouyrie P. Estimating Is Not Measuring: The Lessons About Estimated Pulse Wave Velocity. J Am Heart Assoc. 2022; 11:e025830. https://doi.org/10.1161/JAHA.122.025830 PMID:35535609

4. Justin J, Fayol A, Bruno RM, Khettab H, Boutouyrie P. International Guidelines for Hypertension: Resemblance, Divergence and Inconsistencies. J Clin Med. 2022; 11:1975. https://doi.org/10.3390/jcm11071975 PMID:35407581

5. Duca L, Blaise S, Romier B, Laffargue M, Gayral S, El Btaouri H, Kawecki C, Guillot A, Martiny L, Debelle L, Maurice P. Matrix ageing and vascular impacts: focus on elastin fragmentation. Cardiovasc Res. 2016; 110:298–308. https://doi.org/10.1093/cvr/cvw061 PMID:27009176

6. Prenner SB, Chirinos JA. Arterial stiffness in diabetes mellitus. Atherosclerosis. 2015; 238:370–9. https://doi.org/10.1016/j.atherosclerosis.2014.12.023 PMID:25558032

7. Elias MF, Crichton GE, Dearborn PJ, Robbins MA, Abhayaratna WP. Associations between Type 2 Diabetes Mellitus and Arterial Stiffness: A Prospective Analysis Based on the Maine-Syracuse Study. Pulse (Basel). 2018; 5:88–98. https://doi.org/10.1159/000479560 PMID:29761082

8. Monteiro CI, Simões RP, Goulart CL, Silva CDD, Borghi-Silva A, Mendes RG. Arterial stiffness in type 2 diabetes: determinants and indication of a discriminative value. Clinics (Sao Paulo). 2021; 76:e2172. https://doi.org/10.6061/clinics/2021/e2172 PMID:33624706

9. Mitchell GF. Arterial Stiffness in Aging: Does It Have a Place in Clinical Practice?: Recent Advances in Hypertension. Hypertension. 2021; 77:768–80. https://doi.org/10.1161/HYPERTENSIONAHA.120.14515 PMID:33517682

10. Aroor AR, Jia G, Sowers JR. Cellular mechanisms underlying obesity-induced arterial stiffness. Am J Physiol Regul Integr Comp Physiol. 2018; 314:R387–98. https://doi.org/10.1152/ajpregu.00235.2016 PMID:29167167

11. Wagenseil JE, Mecham RP. Elastin in large artery stiffness and hypertension. J Cardiovasc Transl Res. 2012; 5:264–73. https://doi.org/10.1007/s12265-012-9349-8 PMID:22290157

12. Jacob MP. Extracellular matrix remodeling and matrix metalloproteinases in the vascular wall during aging and in pathological conditions. Biomed Pharmacother. 2003; 57:195–202. https://doi.org/10.1016/s0753-3322(03)00065-9 PMID:12888254

13. Wagenseil JE, Mecham RP. Vascular extracellular matrix and arterial mechanics. Physiol Rev. 2009; 89:957–89. https://doi.org/10.1152/physrev.00041.2008 PMID:19584318

14. Pinto E. Blood pressure and ageing. Postgrad Med J. 2007; 83:109–14. https://doi.org/10.1136/pgmj.2006.048371 PMID:17308214

15. Vouyouka AG, Pfeiffer BJ, Liem TK, Taylor TA, Mudaliar J, Phillips CL. The role of type I collagen in aortic wall strength with a homotrimeric. J Vasc Surg. 2001; 33:1263–70. https://doi.org/10.1067/mva.2001.113579 PMID:11389427

16. Assavarittirong C, Au TY, Nguyen PV, Mostowska A. Vascular Ehlers-Danlos Syndrome: Pathological Variants, Recent Discoveries, and Theoretical Approaches. Cardiol Rev. 2022; 30:308–13. https://doi.org/10.1097/CRD.0000000000000419 PMID:34560710

17. Narayanan N, Pushpakumar SB, Givvimani S, Kundu S, Metreveli N, James D, Bratcher AP, Tyagi SC. Epigenetic regulation of aortic remodeling in hyperhomocysteinemia. FASEB J. 2014; 28:3411–22. https://doi.org/10.1096/fj.14-250183 PMID:24739303

18. Fu S, Li Y, Wu Y, Yue Y, Yang D. Icariside II improves myocardial fibrosis in spontaneously hypertensive rats by inhibiting collagen synthesis. J Pharm Pharmacol. 2020; 72:227–35. https://doi.org/10.1111/jphp.13190 PMID:31820448

19. Li Y, Tai HC, Sladojevic N, Kim HH, Liao JK. Vascular Stiffening Mediated by Rho-Associated Coiled-Coil Containing Kinase Isoforms. J Am Heart Assoc. 2021; 10:e022568. https://doi.org/10.1161/JAHA.121.022568 PMID:34612053

20. Romier B, Dray C, Vanalderwiert L, Wahart A, Hocine T, Dortignac A, Garbar C, Garbar C, Boulagnon C,

Bouland N, Maurice P, Bennasroune A, Sartelet H, et al. Apelin expression deficiency in mice contributes to vascular stiffening by extracellular matrix remodeling of the aortic wall. Sci Rep. 2021; 11:22278. https://doi.org/10.1038/s41598-021-01735-z PMID:34782679

21. Bode MK, Soini Y, Melkko J, Satta J, Risteli L, Risteli J. Increased amount of type III pN-collagen in human abdominal aortic aneurysms: evidence for impaired type III collagen fibrillogenesis. J Vasc Surg. 2000; 32:1201–7. https://doi.org/10.1067/mva.2000.109743 PMID:11107093

22. Wang X, LeMaire SA, Chen L, Shen YH, Gan Y, Bartsch H, Carter SA, Utama B, Ou H, Coselli JS, Wang XL. Increased collagen deposition and elevated expression of connective tissue growth factor in human thoracic aortic dissection. Circulation. 2006; 114:I200–5. https://doi.org/10.1161/CIRCULATIONAHA.105.000240 PMID:16820572

23. Berquand A, Wahart A, Henry A, Gorisse L, Maurice P, Blaise S, Romier-Crouzet B, Pietrement C, Bennasroune A, Sartelet H, Jaisson S, Gillery P, Martiny L, et al. Revealing the elasticity of an individual aortic fiber during ageing at nanoscale by in situ atomic force microscopy. Nanoscale. 2021; 13:1124–33. https://doi.org/10.1039/d0nr06753a PMID:33399602

24. Bergholt MS, Albro MB, Stevens MM. Online quantitative monitoring of live cell engineered cartilage growth using diffuse fiber-optic Raman spectroscopy. Biomaterials. 2017; 140:128–37. https://doi.org/10.1016/j.biomaterials.2017.06.015 PMID:28649013

25. Bergholt MS, Lin K, Wang J, Zheng W, Xu H, Huang Q, Ren JL, Ho KY, Teh M, Srivastava S, Wong B, Yeoh KG, Huang Z. Simultaneous fingerprint and high-wavenumber fiber-optic Raman spectroscopy enhances real-time in vivo diagnosis of adenomatous polyps during colonoscopy. J Biophotonics. 2016; 9:333–42. https://doi.org/10.1002/jbio.201400141 PMID:25850576

26. Heinz A, Huertas AC, Schräder CU, Pankau R, Gosch A, Schmelzer CE. Elastins from patients with Williams-Beuren syndrome and healthy individuals differ on the molecular level. Am J Med Genet A. 2016; 170:1832–42. https://doi.org/10.1002/ajmg.a.37638 PMID:27311421

27. Mora Huertas AC, Schmelzer CE, Hoehenwarter W, Heyroth F, Heinz A. Molecular-level insights into aging processes of skin elastin. Biochimie. 2016; 128-129:163–73. https://doi.org/10.1016/j.biochi.2016.08.010 PMID:27569260

28. Ben Zemzem A, Genevaux A, Wahart A, Bodey AJ, Blaise S, Romier-Crouzet B, Jonquet J, Bour C, Cogranne R, Beauseroy P, Dauchez M, Sherratt MJ, Debelle L, Almagro S. X-ray microtomography reveals a lattice-like network within aortic elastic lamellae. FASEB J. 2021; 35:e21844. https://doi.org/10.1096/fj.202100323RR PMID:34473371

29. Ben Zemzem A, Liang X, Vanalderwiert L, Bour C, Romier-Crouzet B, Blaise S, Sherratt MJ, Weitkamp T, Dauchez M, Baud S, Passat N, Debelle L, Almagro S. Early Alterations of Intra-Mural Elastic Lamellae Revealed by Synchrotron X-ray Micro-CT Exploration of Diabetic Aortas. Int J Mol Sci. 2022; 23:3250. https://doi.org/10.3390/ijms23063250 PMID:35328674

30. Shearer T, Bradley RS, Hidalgo-Bastida LA, Sherratt MJ, Cartmell SH. Three-dimensional visualisation of soft biological structures by X-ray computed micro-tomography. J Cell Sci. 2016; 129:2483–92. https://doi.org/10.1242/jcs.179077 PMID:27278017

31. Wahart A, Hocine T, Albrecht C, Henry A, Sarazin T, Martiny L, El Btaouri H, Maurice P, Bennasroune A, Romier-Crouzet B, Blaise S, Duca L. Role of elastin peptides and elastin receptor complex in metabolic and cardiovascular diseases. FEBS J. 2019; 286:2980–93. https://doi.org/10.1111/febs.14836 PMID:30946528

32. Wagenseil JE, Mecham RP. New insights into elastic fiber assembly. Birth Defects Res C Embryo Today. 2007; 81:229–40. https://doi.org/10.1002/bdrc.20111 PMID:18228265

33. Tsang KM, Knutsen RH, Billington CJ Jr, Lindberg E, Steenbock H, Fu YP, Wardlaw-Pickett A, Liu D, Malide D, Yu ZX, Bleck CKE, Brinckmann J, Kozel BA. Copper-Binding Domain Variation in a Novel Murine Lysyl Oxidase Model Produces Structurally Inferior Aortic Elastic Fibers Whose Failure Is Modified by Age, Sex, and Blood Pressure. Int J Mol Sci. 2022; 23:6749. https://doi.org/10.3390/ijms23126749 PMID:35743192

34. Schräder CU, Heinz A, Majovsky P, Karaman Mayack B, Brinckmann J, Sippl W, Schmelzer CEH. Elastin is

heterogeneously cross-linked. J Biol Chem. 2018; 293:15107–19.
https://doi.org/10.1074/jbc.RA118.004322
PMID:30108173

35. Romier B, Ivaldi C, Sartelet H, Heinz A, Schmelzer CEH, Garnotel R, Guillot A, Jonquet J, Bertin E, Guéant JL, Alberto JM, Bronowicki JP, Amoyel J, et al. Production of Elastin-Derived Peptides Contributes to the Development of Nonalcoholic Steatohepatitis. Diabetes. 2018; 67:1604–15.
https://doi.org/10.2337/db17-0490
PMID:29802129

36. Bako G, Jacob MP, Fulop T Jr, Foris G, Leovey A, Robert L. Immunology of elastin: study of anti-elastin peptide antibodies by DOT immunobinding assay. Immunol Lett. 1987; 15:187–92.
https://doi.org/10.1016/0165-2478(87)90023-x
PMID:3311975

37. Frette C, Wei SM, Neukirch F, Sesboüé R, Martin JP, Jacob MP, Kauffmann F. Relation of serum elastin peptide concentration to age, FEV1, smoking habits, alcohol consumption, and protease inhibitor phenotype: an epidemiological study in working men. Thorax. 1992; 47:937–42.
https://doi.org/10.1136/thx.47.11.937
PMID:1465752

38. Paczek L, Michalska W, Bartlomiejczyk I. Trypsin, elastase, plasmin and MMP-9 activity in the serum during the human ageing process. Age Ageing. 2008; 37:318–23.
https://doi.org/10.1093/ageing/afn039
PMID:18332058

39. Paczek L, Michalska W, Bartlomiejczyk I. Proteolytic enzyme activity as a result of aging. Aging Clin Exp Res. 2009; 21:9–13.
https://doi.org/10.1007/BF03324892
PMID:19225263

40. Mancia G, Fagard R, Narkiewicz K, Redon J, Zanchetti A, Böhm M, Christiaens T, Cifkova R, De Backer G, Dominiczak A, Galderisi M, Grobbee DE, Jaarsma T, et al. 2013 ESH/ESC guidelines for the management of arterial hypertension: the Task Force for the Management of Arterial Hypertension of the European Society of Hypertension (ESH) and of the European Society of Cardiology (ESC). Eur Heart J. 2013; 34:2159–219.
https://doi.org/10.1093/eurheartj/eht151
PMID:23771844

41. Laurent S. Arterial stiffness: intermediate or surrogate endpoint for cardiovascular events? Eur Heart J. 2005; 26:1152–4.
https://doi.org/10.1093/eurheartj/ehi280
PMID:15827059

42. Node K, Kitakaze M, Yoshikawa H, Kosaka H, Hori M. Reduced plasma concentrations of nitrogen oxide in individuals with essential hypertension. Hypertension. 1997; 30:405–8.
https://doi.org/10.1161/01.hyp.30.3.405
PMID:9314424

43. Li P, Schmidt IM, Sabbisetti V, Tio MC, Opotowsky AR, Waikar SS. Plasma Endothelin-1 and Risk of Death and Hospitalization in Patients Undergoing Maintenance Hemodialysis. Clin J Am Soc Nephrol. 2020; 15:784–93.
https://doi.org/10.2215/CJN.11130919
PMID:32381583

44. El-Eshmawy MM, El-Adawy EH, Mousa AA, Zeidan AE, El-Baiomy AA, Abdel-Samie ER, Saleh OM. Elevated serum neutrophil elastase is related to prehypertension and airflow limitation in obese women. BMC Womens Health. 2011; 11:1.
https://doi.org/10.1186/1472-6874-11-1
PMID:21247478

45. Jing Y, Shi J, Lu B, Zhang W, Yang Y, Wen J, Hu R, Yang Z, Wang X. Association of Circulating Cathepsin S and Cardiovascular Disease Among Patients With Type 2 Diabetes: A Cross-Sectional Community-Based Study. Front Endocrinol (Lausanne). 2021; 12:615913.
https://doi.org/10.3389/fendo.2021.615913
PMID:33746900

46. Skjøt-Arkil H, Clausen RE, Rasmussen LM, Wang W, Wang Y, Zheng Q, Mickley H, Saaby L, Diederichsen AC, Lambrechtsen J, Martinez FJ, Hogaboam CM, Han M, et al. Acute Myocardial Infarction and Pulmonary Diseases Result in Two Different Degradation Profiles of Elastin as Quantified by Two Novel ELISAs. PLoS One. 2013; 8:e60936.
https://doi.org/10.1371/journal.pone.0060936
PMID:23805173

47. Ali K, Israr MZ, Ng LL, Mordi I, Lang CC, Kuzmanova E, Huang JT, Choy AM. Plasma desmosine for prediction of outcomes after acute myocardial infarction. Front Cardiovasc Med. 2022; 9:992388.
https://doi.org/10.3389/fcvm.2022.992388
PMID:36479574

48. Mordi IR, Forsythe RO, Gellatly C, Iskandar Z, McBride OM, Saratzis A, Chalmers R, Chin C, Bown MJ, Newby DE, Lang CC, Huang JTJ, Choy AM. Plasma Desmosine and Abdominal Aortic Aneurysm Disease. J Am Heart Assoc. 2019; 8:e013743.
https://doi.org/10.1161/JAHA.119.013743
PMID:31595818

49. Nilsson PM. Genetic and environmental determinants of early vascular ageing (EVA). Curr Vasc Pharmacol. 2012; 10:700–1.

https://doi.org/10.2174/157016112803520981
PMID:23259558

50. Li Y, Gray A, Xue L, Farb MG, Ayalon N, Andersson C, Ko D, Benjamin EJ, Levy D, Vasan RS, Larson MG, Rong J, Xanthakis V, et al. Metabolomic Profiles, Ideal Cardiovascular Health, and Risk of Heart Failure and Atrial Fibrillation: Insights From the Framingham Heart Study. J Am Heart Assoc. 2023; 12:e028022.
https://doi.org/10.1161/JAHA.122.028022
PMID:37301766

51. Lloyd-Jones DM. Cardiovascular risk prediction: basic concepts, current status, and future directions. Circulation. 2010; 121:1768–77.
https://doi.org/10.1161/CIRCULATIONAHA.109.849166
PMID:20404268

52. Liew SM, Doust J, Glasziou P. Cardiovascular risk scores do not account for the effect of treatment: a review. Heart. 2011; 97:689–97.
https://doi.org/10.1136/hrt.2010.220442
PMID:21474616

53. Bramwell JC, Hill AV. The velocity of the pulse wave in man. Proceedings of the royal society B. 1922; 93:298–306.
https://doi.org/10.1098/rspb.1922.0022

54. Brands PJ, Willigers JM, Ledoux LA, Reneman RS, Hoeks AP. A noninvasive method to estimate pulse wave velocity in arteries locally by means of ultrasound. Ultrasound Med Biol. 1998; 24:1325–35.
https://doi.org/10.1016/s0301-5629(98)00126-4
PMID:10385955

55. Maizel J, Six I, Slama M, Tribouilloy C, Sevestre H, Poirot S, Giummelly P, Atkinson J, Choukroun G, Andrejak M, Kamel S, Mazière JC, Massy ZA. Mechanisms of aortic and cardiac dysfunction in uremic mice with aortic calcification. Circulation. 2009; 119:306–13.
https://doi.org/10.1161/CIRCULATIONAHA.108.797407
PMID:19118252

56. Blaise S, Romier B, Kawecki C, Ghirardi M, Rabenoelina F, Baud S, Duca L, Maurice P, Heinz A, Schmelzer CE, Tarpin M, Martiny L, Garbar C, et al. Elastin-derived peptides are new regulators of insulin resistance development in mice. Diabetes. 2013; 62:3807–16.
https://doi.org/10.2337/db13-0508
PMID:23919962

57. Nave AH, Mižíková I, Niess G, Steenbock H, Reichenberger F, Talavera ML, Veit F, Herold S, Mayer K, Vadász I, Weissmann N, Seeger W, Brinckmann J, Morty RE. Lysyl oxidases play a causal role in vascular remodeling in clinical and experimental pulmonary arterial hypertension. Arterioscler Thromb Vasc Biol. 2014; 34:1446–58.
https://doi.org/10.1161/ATVBAHA.114.303534
PMID:24833797

58. Doué M, Okwieka A, Berquand A, Gorisse L, Maurice P, Velard F, Terryn C, Molinari M, Duca L, Piétrement C, Gillery P, Jaisson S. Carbamylation of elastic fibers is a molecular substratum of aortic stiffness. Sci Rep. 2021; 11:17827.
https://doi.org/10.1038/s41598-021-97293-5
PMID:34497312

SUPPLEMENTARY MATERIALS

Supplementary Methods

Functional parameters

Measurement of blood pressure

Currently, multiple more or less invasive methods exist to study blood pressure in animals. In our case we have chosen the tail-cuff method, which is non-invasive and the closest to those measurements taken in humans. Other available methods require anesthesia and/or delicate surgery and are not suitable for the study of aortic remodeling. However, the tail-cuff method requires adaptation of the animals, handling, restraint and swelling of the sleeve of the Sphygmomanometer. Regularization is carried out every day, one week before the test. The final measurement is the average of five successive measurements as described in [1, 2]. Three parameters were analyzed, the pulse, the systolic (SBP) and diastolic (DBP) blood pressures. From these, the mean arterial pressure (MAP) and the pulsed pressure (PP) can be deduced from: PAM = 2/3 PAD + 1/3 PAS; PP = PAS – PAD. If the SBP and/or DBP of aged C57Bl/6 were statistically superior to the pressure of the young C57Bl/6 mice, then we considered the mice to be hypertensive.

Pulse wave velocity (PWV)

The velocity measurement is done in anesthetized animals (4% isoflurane, 10 min). The measurement can be made either from ultrasound probes (Indus Instruments, Webster, TX, USA), one placed at the level of the aortic arch and the other at the level of the abdominal thoracic aorta near the bifurcation of the iliac arteries. While the Doppler ultrasound system can measure a velocity limited to portions of arteries (carotids, aortic arch), this method considers the entire aorta and gives a more general idea of the rigidity of the vessel.

High-frequency ultrasound imaging

High resolution ultrasound imaging was performed with anesthetized animals (isoflurane 4%). The animals were depilated with hair removal cream and placed on a heated table (37°C). For ultrasound measurements, a Vevo3000 ultrasound imaging system (VisualSonics, Toronto, Canada) with a 30 MHz linear signal transducer was used for measurements of anatomical and functional parameters of left ventricle of heart needed to determine factors such as ejection fraction, cardiac output, fractional area change, fractional shortening, stroke volume, end-systolic volume (LVESV), and end-diastolic volume (LVEDV). At the level of the aortic arch, the diameter of the vessel was measured during the cardiac cycle (systole, Ds-diastole, Dd), as well as the pulse wave velocity (PWV) and the thickness of the tunica intima-media (h). Distensibility factor (DC) and Young's modulus (E) were derived by Bramwell and Hill [3] equation ($PWV = \sqrt{\frac{E \times h}{D \times \rho}}$) and Moens-Korteweg equation ($PWV = \sqrt{\frac{1}{\rho \times DC}}$), respectively. From the conclusions of Brands et al. [4], the local variation of the pressure during the cardiac cycle (DP) and the compliance (CC) can then be deduced as: $\Delta P = \frac{\frac{(As - Ad)}{Ad}}{DC}$ et $CC = \frac{(As - Ad)}{\Delta P}$. Additional information is available in the Supplementary Materials section.

Vascular reactivity

We investigated the effects of aging on *ex vivo* aortic reactivity. Wild-type mice were anesthetized by intraperitoneal injections of pentobarbital sodium (150 mg/kg). Once euthanasia was complete, their hearts were removed. Vascular reactivity studies were carried out, as described in [5]. A midline incision was made through the sternum to open up the thoracic cavity, and the descending thoracic aorta was carefully isolated. Each aorta was sectioned into 3.5 mm rings devoid of fat and connective tissue. The rings were placed in Kreb's-Henseleit (KH) solution under 5% CO_2 and 95% O_2 atmosphere at 37°C. The aorta rings were maintained under a 1.3 g tension (previously determined as the optimal point for their length-tension relationship) and allowed to equilibrate for 1 h. All rings were pre-constricted with potassium chloride (KCl). After rinsing, phenylephrine (between 10^{-9} and 3.10^{-5} mol/L) was added to the medium. The constriction was expressed as a percentage of the KCl response. The endothelium function was measured as the relaxation response to acetylcholine (between 10^{-9} and 3.10^{-5} mol/L). The degree of relaxation was calculated considering the maximal contraction obtained with phenylephrine.

Biochemical parameters

Cross-linking assay

Protein analysis was performed as described in [6]. Briefly, for collagen crosslink analysis, samples were reduced by sodium borohydride (Sigma, Germany; 25 mg $NaBH_4$/ml in 0.05 M NaH_2PO_4/0.15 M NaCl pH

7.4, 1 h on ice, 1.5 h at room temperature) and digested with high purity bacterial collagenase (C0773; Sigma, Germany; 50 U/ml, 37°C, 12 h). The soluble fractions containing collagen cross-links were hydrolyzed in 6 N HCl at 110°C for 24 h. The hydrolysates were precleared by solid phase extraction. Dried eluates were analyzed on an amino acid analyzer (Biochrom 30, Biochrom, Cambridge, UK). The nomenclature of the crosslinks used in the article refers to the reduced variants of crosslinks. The collagen content was analyzed in an aliquot of hydrolyzed samples of the collagenase soluble fraction prior to preclearance and calculated based on a content of 14 mg hydroxyproline in 100 mg collagen. For protein and elastin crosslinks analysis, samples were digested with bacterial collagenase [7]. The soluble fraction containing collagen was subjected to hydrolysis and amino acid analysis. The residual fraction was extracted by hot alkali (0.1 N NaOH, 95°C, 45 min). The supernatant containing non-collagenous/non-elastin proteins and the insoluble residue containing insoluble elastin were subjected to hydrolysis and amino acid analysis. The content of elastin crosslinks was analyzed in an aliquot of the NaOH-insoluble fraction containing elastin after CF-11 preclearance by amino acid analysis.

Gene expression

Was analyzed by qPCR, as previously described [20]. Total RNA was extracted using Trizol reagent (Eurobio Scientific, Les Ulis, France). The RNA concentration was measured using a NanoDrop system (Thermo Fisher Scientific, Illkirch, France). The 260/280 ratio was calculated, using NanoDrop software, to evaluate protein contamination. Complementary DNA (cDNA) was generated using a Verso cDNA kit (Thermo Fisher Scientific, Illkirch, France). Real-time PCR was performed using SYBR Green on a BioRad CFX96 Real-Time System (Bio-Rad, Hercules, CA, USA). In this study, 5 µl cDNA (1/10) and 0.7 µl of each forward and reverse primer (3 µM) were used for the qPCR test, with cycling conditions as follows: 95°C for 15 minutes, 40 cycles of 95°C for 10 seconds, and 60°C for 60 seconds. RNA expression was normalized to the housekeeping genes 36B4 and RPS26, and relative gene expression was calculated using the 2−ΔΔCT method. Supplementary Table 2 presents the forward and reverse sequences.

Imaging parameters

Raman spectroscopy/imaging

Raman measurements were performed with a Witec alpha 300R confocal Raman microscope (Witec GmbH, Ulm, Germany). Paraffin cross-sections (3 µm thickness) of aortas underwent deparaffinization by a consecutive row of xylene and ethanol steps and were rehydrated in PBS. Samples were kept hydrated during the entire measurement. For each sample, two images were acquired of an area of 80 × 90 µm, at a spatial resolution of 0.5 × 0.5 µm/pixel and an integration time of 0.05 s/spectrum. A green laser (532 nm) with an output power of 60 mW, a 600 g/mm grating and a 63× water dipping objective were selected for the measurements. Sections from 7 animals were measured for each group.

Data analysis

First, data were preprocessed by cosmic ray removal, baseline correction (shape algorithm), cropping to the wavenumber region between 300–3000 cm^{-1} and normalizing (area to 1 normalization). True component analysis (TCA, Witec Project 5.2 Software) was performed for image generation. Briefly, the TCA algorithm identifies most prevalent spectral signatures in the Raman maps, the corresponding pixel and thus allows to generate intensity distribution heatmaps for each component. For further in-depth analysis of molecular changes, single spectra were extracted from the preprocessed TCA images and analyzed by principal component analysis (PCA). PCA allows to decompose the spectral information to a defined number of vectors (principal components, PC), which elaborate spectral similarities and differences that can be explained by the corresponding loadings plot. PCA was performed for elastic fibers and the interfibrillar ECM. 400 spectra were extracted per animal and applied for PCA. Statistical analysis was performed by comparing the average score values of each animal (GraphPad Prism 9, unpaired t-test).

Atomic Force Microscopy (AFM)

Frozen 10 µm-thick aorta cross-sections were incubated in KH solution for equilibration at 37°C. The prepared samples were put onto the microscope stage and observed with bright field illumination to locate the spots of interest. Analysis was performed using AFM (Bioscope Catalyst, Bruker, Billerica, MA, USA, driven by the Nanoscope Analysis 1.8 software) coupled to a Nikon Eclipse Ti inverted microscope (Nikon, Tokyo, Japan). To obtain a representative set of values for each cross section, AFM analyses were performed at three different locations of the cross section, and each experiment was triplicated, leading to nine different areas analyzed per condition. Experiments were performed in the KH buffer using the Peak Force Quantitative NanoMechanical (PFQNM) mode with ScanAsyst-air probes (Bruker, Billerica, MA, USA) with a nominal spring constant of 0.4 N/m and a nominal resonant frequency of 70 kHz. For the PFQNM calibration, the standard supplier protocol was applied

to obtain quantitative measurements of the Young's modulus (YM). First, the deflection sensitivity was calibrated, before use in the buffer, by carrying out indentation ramps on a clean and hard sapphire surface. Then, the cantilever spring constant was calculated before and after each experiment, following the thermal tuning method. The last step was to calibrate the curvature radius of the tip using a standard titanium tip check sample. This curvature radius was confirmed by performing a test measurement of the YM of a calibrated known sample. A PeakForce frequency of 0.25 kHz was used to maximize the contact time between the tip and the sample, and the PeakForce amplitude was set to 2 µm. The distance synchronization parameter was manually and constantly adjusted over time so that the turnaway point of each force curve was exactly at the (x, y) maximum position. Images were captured with a resolution of 256 pixels per line. Once the different AFM images were acquired, the force curves were extracted from chosen areas in the PFQNM images for the YM calculation, and the conventional Derjaguin–Muller–Toporov (DMT) model was used to fit the linear part of the extension curve, as it was identified as the best suited model according to the tip geometry and the properties of the samples. The YM at each point of the elastic fibers or of the inter-fiber spaces was calculated using a value of the Poisson ratio of 0.5 for our samples considered incompressible. For each condition, at least 5000 force curves were treated to obtain the mean values of the YM for the elastic fibers and the inter-fiber spaces. The analyses were performed at three different locations in each cross-section, for a total of nine cross-sections obtained from three different mice.

High-resolution X-ray microscopy

Sample preparation

Aorta specimens from 6-month-old mice (n = 4) and 20-months-old mice (n = 4) were received embedded in paraffin. The paraffin was removed by immersion in xylene for 30 min, followed by staining with a 0.5% I_2 in ethanol solution for 30 min. After immersion in xylene once again for 30 min, the sample was embedded in paraffin and, using a heated blade, it was manually cut into sections of ca 500 µm thickness orthogonal to the aorta longest axis. Afterwards, the sample was glued onto the tip of a metallic pin with the aid of a stereo microscope.

X-ray imaging

A Carl Zeiss Xradia 810 Ultra X-ray microscope equipped with a chromium source (5.4 keV) was used in the imaging experiments. The sample located onto the tip of a metallic pin was inserted in the sample holder of the device and the experiments were performed using Zernike phase-contrast. Samples were scanned using a field-of-view of 64 µm^2. A total of 901 projection images, with an exposure time of 20 s each, were acquired by rotating the sample over 180°. Each sample was imaged for two or more times, and the reconstructed volumetric images were stitched after reconstruction. Image reconstruction was performed by a filtered back-projection algorithm using the XMReconstructor software integrated into the Xradia 810 Ultra and the final images have isotropic voxel size of 128 nm. The tomograms obtained were exported as a stack of 16-bit TIFF images for stitching and visualization in Thermo Fischer Avizo software (version 3D 2021.1).

Scanning electron microscopy

Defrosted samples were deposited onto a SEM stub and treated with NanoSuit® Aqueous Solution (Electron Microscopy Sciences) according to the manufacturer instructions. Samples were imaged in a Scanning Electron Microscope FEI Quanta 3D FEG Dual-Beam working at an acceleration voltage of 5 kV.

Supplementary References

1. Romier B, Dray C, Vanalderwiert L, Wahart A, Hocine T, Dortignac A, Garbar C, Garbar C, Boulagnon C, Bouland N, Maurice P, Bennasroune A, Sartelet H, et al. Apelin expression deficiency in mice contributes to vascular stiffening by extracellular matrix remodeling of the aortic wall. Sci Rep. 2021; 11:22278. https://doi.org/10.1038/s41598-021-01735-z PMID:34782679

2. Berquand A, Wahart A, Henry A, Gorisse L, Maurice P, Blaise S, Romier-Crouzet B, Pietrement C, Bennasroune A, Sartelet H, Jaisson S, Gillery P, Martiny L, et al. Revealing the elasticity of an individual aortic fiber during ageing at nanoscale by in situ atomic force microscopy. Nanoscale. 2021; 13:1124–33. https://doi.org/10.1039/d0nr06753a PMID:33399602

3. Bramwell JC. The velocity of the pulse wave in man. Proceedings of the royal society B. 1922; 93: 298–306.

4. Brands PJ, Willigers JM, Ledoux LA, Reneman RS, Hoeks AP. A noninvasive method to estimate pulse wave velocity in arteries locally by means of ultrasound. Ultrasound Med Biol. 1998; 24:1325–35. https://doi.org/10.1016/s0301-5629(98)00126-4 PMID:10385955

5. Maizel J, Six I, Slama M, Tribouilloy C, Sevestre H, Poirot S, Giummelly P, Atkinson J, Choukroun G, Andrejak M, Kamel S, Mazière JC, Massy ZA.

Mechanisms of aortic and cardiac dysfunction in uremic mice with aortic calcification. Circulation. 2009; 119:306–13.
https://doi.org/10.1161/CIRCULATIONAHA.108.797407
PMID:19118252

6. Nave AH, Mižíková I, Niess G, Steenbock H, Reichenberger F, Talavera ML, Veit F, Herold S, Mayer K, Vadász I, Weissmann N, Seeger W, Brinckmann J, Morty RE. Lysyl oxidases play a causal role in vascular remodeling in clinical and experimental pulmonary arterial hypertension. Arterioscler Thromb Vasc Biol. 2014; 34:1446–58.
https://doi.org/10.1161/ATVBAHA.114.303534
PMID:24833797

7. Leray C, Pelletier X, Hemmendinger S, Cazenave JP. Thin-layer chromatography of human platelet phospholipids with fatty acid analysis. J Chromatogr. 1987; 420:411–6.
https://doi.org/10.1016/0378-4347(87)80198-6
PMID:3693512

8. Henry JP, Meehan JP, Stephens P, Santisteban GA. Arterial pressure in cba mice as related to age. J Gerontol. 1965; 20:239–43.
https://doi.org/10.1093/geronj/20.2.239
PMID:14284803

9. Pezet M, Jacob MP, Escoubet B, Gheduzzi D, Tillet E, Perret P, Huber P, Quaglino D, Vranckx R, Li DY, Starcher B, Boyle WA, Mecham RP, Faury G. Elastin haploinsufficiency induces alternative aging processes in the aorta. Rejuvenation Res. 2008; 11:97–112.
https://doi.org/10.1089/rej.2007.0587
PMID:18173368

10. Mariko B, Pezet M, Escoubet B, Bouillot S, Andrieu JP, Starcher B, Quaglino D, Jacob MP, Huber P, Ramirez F, Faury G. Fibrillin-1 genetic deficiency leads to pathological ageing of arteries in mice. J Pathol. 2011; 224:33–44.
https://doi.org/10.1002/path.2840
PMID:21432852

11. Elias MF, Pentz CA 3rd. Blood pressure extremes and activity in aging mice. Physiol Behav. 1977; 19:811–3.
https://doi.org/10.1016/0031-9384(77)90320-1
PMID:609621

12. Sonesson B, Hansen F, Stale H, Länne T. Compliance and diameter in the human abdominal aorta--the influence of age and sex. Eur J Vasc Surg. 1993; 7:690–7.
https://doi.org/10.1016/s0950-821x(05)80718-2
PMID:8270073

13. Lakatta EG, Levy D. Arterial and cardiac aging: major shareholders in cardiovascular disease enterprises: Part II: the aging heart in health: links to heart disease. Circulation. 2003; 107:346–54.
https://doi.org/10.1161/01.cir.0000048893.62841.f7
PMID:12538439

14. Lakatta EG, Levy D. Arterial and cardiac aging: major shareholders in cardiovascular disease enterprises: Part I: aging arteries: a "set up" for vascular disease. Circulation. 2003; 107:139–46.
https://doi.org/10.1161/01.cir.0000048892.83521.58
PMID:12515756

15. Lakatta EG. Arterial and cardiac aging: major shareholders in cardiovascular disease enterprises: Part III: cellular and molecular clues to heart and arterial aging. Circulation. 2003; 107:490–7.
https://doi.org/10.1161/01.cir.0000048894.99865.02
PMID:12551876

16. Greenwald SE. Ageing of the conduit arteries. J Pathol. 2007; 211:157–72.
https://doi.org/10.1002/path.2101
PMID:17200940

17. Jadidi M, Habibnezhad M, Anttila E, Maleckis K, Desyatova A, MacTaggart J, Kamenskiy A. Mechanical and structural changes in human thoracic aortas with age. Acta Biomater. 2020; 103:172–88.
https://doi.org/10.1016/j.actbio.2019.12.024
PMID:31877371

18. Kawel-Boehm N, Hetzel SJ, Ambale-Venkatesh B, Captur G, Francois CJ, Jerosch-Herold M, Salerno M, Teague SD, Valsangiacomo-Buechel E, van der Geest RJ, Bluemke DA. Reference ranges ("normal values") for cardiovascular magnetic resonance (CMR) in adults and children: 2020 update. J Cardiovasc Magn Reson. 2020; 22:87.
https://doi.org/10.1186/s12968-020-00683-3
PMID:33308262

19. Gharraee N, Sun Y, Swisher JA, Lessner SM. Age and sex dependency of thoracic aortopathy in a mouse model of Marfan syndrome. Am J Physiol Heart Circ Physiol. 2022; 322:H44–56.
https://doi.org/10.1152/ajpheart.00255.2021
PMID:34714692

20. Wheeler JB, Mukherjee R, Stroud RE, Jones JA, Ikonomidis JS. Relation of murine thoracic aortic structural and cellular changes with aging to passive and active mechanical properties. J Am Heart Assoc. 2015; 4:e001744.
https://doi.org/10.1161/JAHA.114.001744
PMID:25716945

21. Hemmeryckx B, Hoylaerts MF, Deloose E, Van Hove CE, Fransen P, Bult H, Lijnen HR. Age-associated pro-inflammatory adaptations of the mouse thoracic aorta. Thromb Haemost. 2013; 110:785–94.

https://doi.org/10.1160/TH13-01-0022
PMID:23925372

22. Cavinato C, Murtada SI, Rojas A, Humphrey JD. Evolving structure-function relations during aortic maturation and aging revealed by multiphoton microscopy. Mech Ageing Dev. 2021; 196:111471. https://doi.org/10.1016/j.mad.2021.111471 PMID:33741396

23. Sokolis DP. Time-course of axial residual strain remodeling and layer-specific thickening during aging along the human aorta. J Biomech. 2020; 112:110065. https://doi.org/10.1016/j.jbiomech.2020.110065 PMID:33035841

24. Kelleher CM, McLean SE, Mecham RP. Vascular extracellular matrix and aortic development. Curr Top Dev Biol. 2004; 62:153–88. https://doi.org/10.1016/S0070-2153(04)62006-0 PMID:15522742

25. Fritze O, Romero B, Schleicher M, Jacob MP, Oh DY, Starcher B, Schenke-Layland K, Bujan J, Stock UA. Age-related changes in the elastic tissue of the human aorta. J Vasc Res. 2012; 49:77–86. https://doi.org/10.1159/000331278 PMID:22105095

26. Liu SL, Bae YH, Yu C, Monslow J, Hawthorne EA, Castagnino P, Branchetti E, Ferrari G, Damrauer SM, Puré E, Assoian RK. Matrix metalloproteinase-12 is an essential mediator of acute and chronic arterial stiffening. Sci Rep. 2015; 5:17189. https://doi.org/10.1038/srep17189 PMID:26608672

27. Hornebeck W, Adnet JJ, Robert L. Age dependent variation of elastin and elastase in aorta and human breast cancers. Exp Gerontol. 1978; 13:293–8. https://doi.org/10.1016/0531-5565(78)90037-2 PMID:738376

28. McNulty M, Spiers P, McGovern E, Feely J. Aging is associated with increased matrix metalloproteinase-2 activity in the human aorta. Am J Hypertens. 2005; 18:504–9. https://doi.org/10.1016/j.amjhyper.2004.11.011 PMID:15831360

29. Leloup AJ, Van Hove CE, Heykers A, Schrijvers DM, De Meyer GR, Fransen P. Elastic and Muscular Arteries Differ in Structure, Basal NO Production and Voltage-Gated Ca(2+)-Channels. Front Physiol. 2015; 6:375. https://doi.org/10.3389/fphys.2015.00375 PMID:26696904

30. Ng HH, Jelinic M, Parry LJ, Leo CH. Increased superoxide production and altered nitric oxide-mediated relaxation in the aorta of young but not old male relaxin-deficient mice. Am J Physiol Heart Circ Physiol. 2015; 309:H285–96. https://doi.org/10.1152/ajpheart.00786.2014 PMID:25957220

31. Al-Shaer MH, Choueiri NE, Correia ML, Sinkey CA, Barenz TA, Haynes WG. Effects of aging and atherosclerosis on endothelial and vascular smooth muscle function in humans. Int J Cardiol. 2006; 109:201–6. https://doi.org/10.1016/j.ijcard.2005.06.002 PMID:16054252

32. Andrawis N, Jones DS, Abernethy DR. Aging is associated with endothelial dysfunction in the human forearm vasculature. J Am Geriatr Soc. 2000; 48:193–8. PMID:10682949

33. Blackwell KA, Sorenson JP, Richardson DM, Smith LA, Suda O, Nath K, Katusic ZS. Mechanisms of aging-induced impairment of endothelium-dependent relaxation: role of tetrahydrobiopterin. Am J Physiol Heart Circ Physiol. 2004; 287:H2448–53. https://doi.org/10.1152/ajpheart.00248.2004 PMID:15319209

34. Novella S, Dantas AP, Segarra G, Vidal-Gómez X, Mompeón A, Garabito M, Hermenegildo C, Medina P. Aging-related endothelial dysfunction in the aorta from female senescence-accelerated mice is associated with decreased nitric oxide synthase expression. Exp Gerontol. 2013; 48:1329–37. https://doi.org/10.1016/j.exger.2013.08.003 PMID:23948180

35. Donato AJ, Magerko KA, Lawson BR, Durrant JR, Lesniewski LA, Seals DR. SIRT-1 and vascular endothelial dysfunction with ageing in mice and humans. J Physiol. 2011; 589:4545–54. https://doi.org/10.1113/jphysiol.2011.211219 PMID:21746786

36. Gerhard M, Roddy MA, Creager SJ, Creager MA. Aging progressively impairs endothelium-dependent vasodilation in forearm resistance vessels of humans. Hypertension. 1996; 27:849–53. https://doi.org/10.1161/01.hyp.27.4.849 PMID:8613259

37. Taddei S, Virdis A, Mattei P, Ghiadoni L, Fasolo CB, Sudano I, Salvetti A. Hypertension causes premature aging of endothelial function in humans. Hypertension. 1997; 29:736–43. https://doi.org/10.1161/01.hyp.29.3.736 PMID:9052889

38. Huynh J, Nishimura N, Rana K, Peloquin JM, Califano JP, Montague CR, King MR, Schaffer CB, Reinhart-King CA. Age-related intimal stiffening enhances

endothelial permeability and leukocyte transmigration. Sci Transl Med. 2011; 3:112ra122. https://doi.org/10.1126/scitranslmed.3002761 PMID:22158860

39. Lee K, Saidel GM, Penn MS. Permeability change of arterial endothelium is an age-dependent function of lesion size in apolipoprotein E-null mice. Am J Physiol Heart Circ Physiol. 2008; 295:H2273–9. https://doi.org/10.1152/ajpheart.00242.2008 PMID:18835923

40. Carlson KH, Bourne WM, McLaren JW, Brubaker RF. Variations in human corneal endothelial cell morphology and permeability to fluorescein with age. Exp Eye Res. 1988; 47:27–41. https://doi.org/10.1016/0014-4835(88)90021-8 PMID:3409985

41. Krettek A, Sukhova GK, Libby P. Elastogenesis in human arterial disease: a role for macrophages in disordered elastin synthesis. Arterioscler Thromb Vasc Biol. 2003; 23:582–7. https://doi.org/10.1161/01.ATV.0000064372.78561.A5 PMID:12615674

42. Docherty JR, O'Malley K. Ageing and alpha-adrenoceptors. Clin Sci (Lond). 1985; 68:133s–36. https://doi.org/10.1042/cs068s133 PMID:2857609

43. Elliott HL, Sumner DJ, McLean K, Reid JL. Effect of age on the responsiveness of vascular alpha-adrenoceptors in man. J Cardiovasc Pharmacol. 1982; 4:388–92. https://doi.org/10.1097/00005344-198205000-00008 PMID:6177934

44. Fenton M, Huang HL, Hong Y, Hawe E, Kurz DJ, Erusalimsky JD. Early atherogenesis in senescence-accelerated mice. Exp Gerontol. 2004; 39:115–22. https://doi.org/10.1016/j.exger.2003.10.004 PMID:14724071

45. Li Y, Gilbert TR, Matsumoto AH, Shi W. Effect of aging on fatty streak formation in a diet-induced mouse model of atherosclerosis. J Vasc Res. 2008; 45:205–10. https://doi.org/10.1159/000112133 PMID:18063868

46. Simo OK, Berrougui H, Fulop T, Khalil A. The Susceptibility to Diet-Induced Atherosclerosis Is Exacerbated with Aging in C57B1/6 Mice. Biomedicines. 2021; 9:487. https://doi.org/10.3390/biomedicines9050487 PMID:33946646

47. Tyrrell DJ, Blin MG, Song J, Wood SC, Zhang M, Beard DA, Goldstein DR. Age-Associated Mitochondrial Dysfunction Accelerates Atherogenesis. Circ Res. 2020; 126:298–314. https://doi.org/10.1161/CIRCRESAHA.119.315644 PMID:31818196

48. Yagi K, Komura S, Sasaguri Y, Yoshino K, Ohishi N. Atherogenic change in the thoracic aorta of the senescence-accelerated mouse. Atherosclerosis. 1995; 118:233–6. https://doi.org/10.1016/0021-9150(95)05609-2 PMID:8770317

49. Fernández-Friera L, Peñalvo JL, Fernández-Ortiz A, Ibañez B, López-Melgar B, Laclaustra M, Oliva B, Mocoroa A, Mendiguren J, Martínez de Vega V, García L, Molina J, Sánchez-González J, et al. Prevalence, Vascular Distribution, and Multiterritorial Extent of Subclinical Atherosclerosis in a Middle-Aged Cohort: The PESA (Progression of Early Subclinical Atherosclerosis) Study. Circulation. 2015; 131:2104–13. https://doi.org/10.1161/CIRCULATIONAHA.114.014310 PMID:25882487

50. Paydary K, Revheim ME, Emamzadehfard S, Gholami S, Pourhassan S, Werner TJ, Høilund-Carlsen PF, Alavi A. Quantitative thoracic aorta calcification assessment by ^{18}F-NaF PET/CT and its correlation with atherosclerotic cardiovascular disorders and increasing age. Eur Radiol. 2021; 31:785–94. https://doi.org/10.1007/s00330-020-07133-9 PMID:32870396

Supplementary Figures

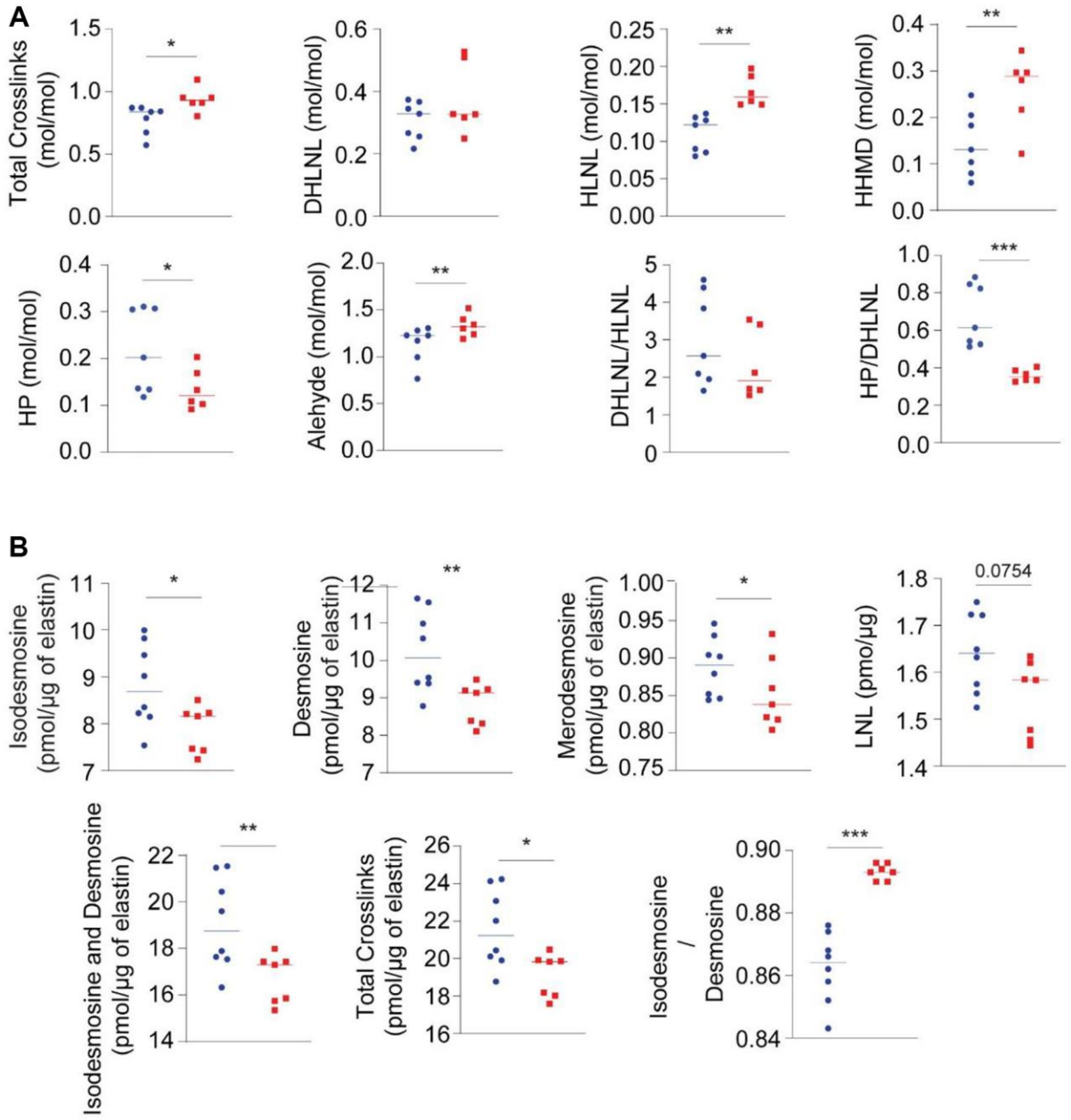

Supplementary Figure 1. Evaluation of crosslinks in abdominal aorta of young (blue) or old (red) mice. (**A**) Collagen cross-links. (**B**) Elastin cross-links. Statistical test: Mann-Whitney. Mean +/− SEM. Significant differences ($^{*}p < 0.05$, $^{**}p < 0.001$, $^{***}p < 0.0001$, Mann-Whitney).

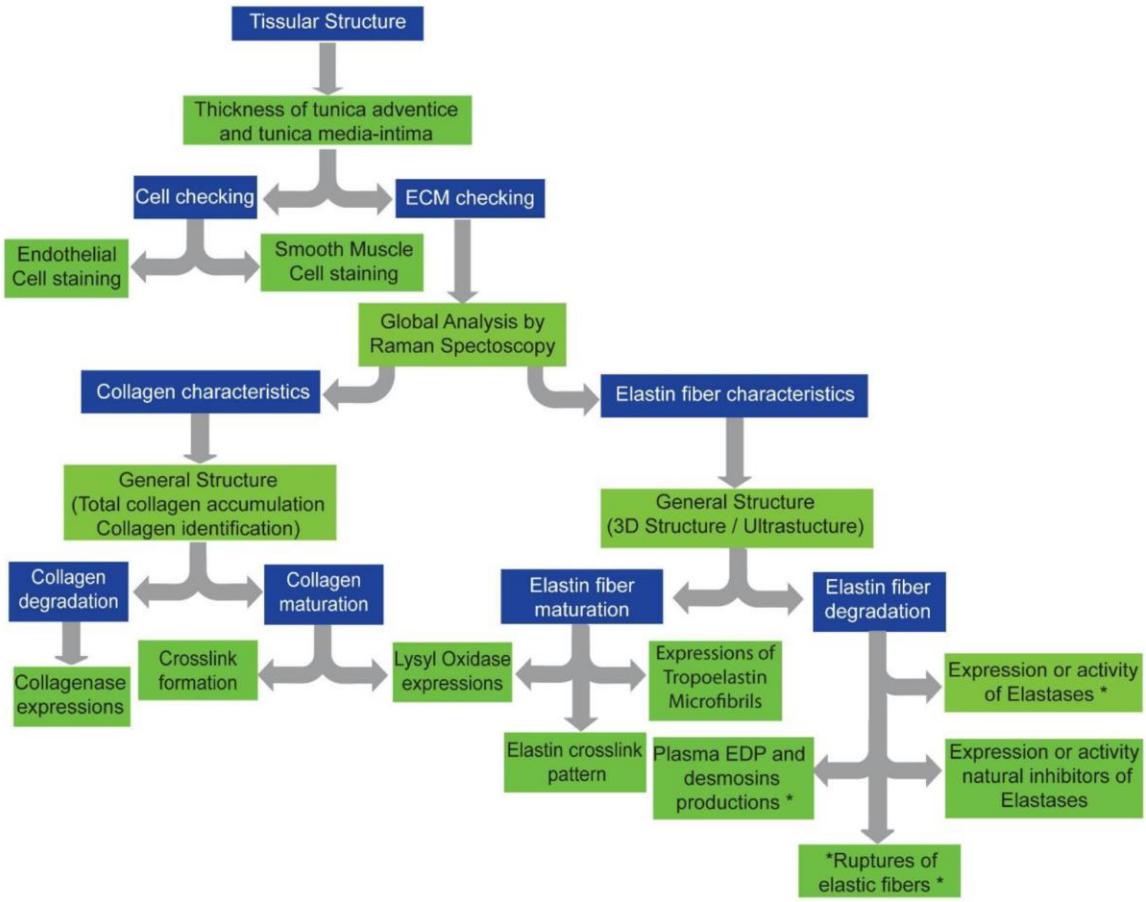

Supplementary Figure 2. Summary of the decision tree allowing the study of vascular stiffness by morphological approaches. "*" identifies parameters that are methodologically accessible for clinical studies.

Supplementary Tables

Supplementary Table 1. Variations of aortic parameters from young to aged in mice and humans.

	Mouse	Human
Systolic blood pressure (mmHg)	= or ↑ [8–11]	↑ [12, 13]
Aortic stiffness	↑ [9, 10, 14]	↑ [12, 13, 15–18]
Aortic structure		
Lumen diameter	↑ [9, 10, 19, 21]	↑ [12, 15, 16, 18]
Wall thickness	↑ [9, 10, 20, 21]	↑ [14–17]
Number of elastic lamellae	= [9, 10]	= [17]
Adventitia thickness	= [22]	= [23]
Elastic fiber-related processes in the aortic wall		
Elastogenesis	↓ [24]	↓ [25]
Elastolysis	↑ [26]	= or ↑ [25, 27, 28]
Endothelial cell function		
Basal NO production	↓ [21, 29, 30]	↓ (Dilation of forearm arteries) [31, 32]
Acetylcholine-triggered NO production	↓ [21, 30, 33, 34]	↓ (Dilation of forearm arteries) [15, 35–37]
Permeability	↑ [38, 39]	↑ (Corneal endothelial cells) [40]
Vascular smooth muscle cell function		
Elastin production	↓ [24]	↓ [25, 41]
Contractility	↓, = or ↑ [9, 10, 20, 21, 34]	↓, = or ↑ [42, 43]
Susceptibility to atherogenesis	↑ or = [44–48]	↑ [13, 49, 50]
Left ventricular hypertrophy (LVH)	↑ [9]	↑ [13]

The complete list of references (here in brackets) can be found in the supplementary section.

Supplementary Table 2. Sequences used for qPCR.

Gene name	Forward sequence (5′ → 3′)	Reverse sequence (5′ → 3′)
RPS26	TAGAAGCCGCTGCTGTCAGG	GGCACAGCTCACGCAATAATG
36B4	AAAGCCTGGAAGAAGGAGGTC	AGATTCGGGATATGCTGTTGG
MMP-1	CACTCCCTTGGGCTCACTCA	GTTGCACCTGTTGGCTGGAT
MMP-2	ATCGAGACCATGCGGAAGC	GCCCGAGCAAAAGCATCAT
MMP-8	AACGGGAAGACATAC	GGGTCCATGGATCTT
MMP-9	CACGGAGACGGGTATCCCTT	GGGCACCATTTGAGTTTCCAT
MMP13	CAGTCTCCGAGGAGAAACTATGAT	GGACTTTGTCAAAAAGAGCTCAG
Myosin light-chain kinase (M*LCK*)	TGGGGGACGTGAAACTGTTTG	GGGGCAGAATGAAAGCTGG
Neutrophil elastase (NE)	TGGAGGTCATTTCTGTGGTG	CTGCACTGACCGGAAATTTAG
Cathepsin-S	GCGTCACTGAGGTGAAATACC	CCCCCACAGCACTGAAAG
Cystatin C	ATGACCAGCCCCATCTGA	CCAGGGCACGCTGTAGAT
Tissue inhibitors of metalloproteinase (Timp1)	TCCCCAGAAATCAACGAGACC	GTACCGGATATCTGCGGCATT
Serine peptidase inhibitor (SERPIN)	TAGGGAGCAAGGGTGACACTC	ACTGTCTGGTCTGTTGAGGGT
Elastin (ELN)	GCTGCTGCTAAGGCTGCTAA	AGCACCTGGGAGCCTAACTC
Fibrillin 1 (FBN1)	GGACGGAAAGAACTGTGAAGAT	ACACATTCCGTTTAGGCACA
Fibulin 5 (FBLN5)	ATCTGCTGATTGGTGAAAACC	ATGGTGAATGGCTGGTCTCT
Lysyl oxidase like 1 (LOXL1)	GAATACTGAGCCAGACTGGC	GGGTCTCATTGAAATTAGTATCC
Lysyl oxidase like 2 (LOXL2)	ATGACCTGCTGAGCCTCAAC	CAGTGTCCTCCAGGCAGAAG
Lysyl oxidase like 3 (LOXL3)	ATGGGTGCCATCCACTTGAG	TGTTCTTGGACGGGCATCTC
Lysyl oxidase like 4 (LOXL4)	GGTTGTGAACCCCACAAACG	CTGCATTGGCTCGGTAGGAA

Lysyl oxidase (LOX)	CTATTCGATCCCACGCTGCT	CCTCACAATGGGGATGTGCT
Latent TGF beta binding protein (Ltbp-4)	CGTCAACGAGTGTGATGAGG	GAGCAAATCCTGGACGACAG
Smooth muscle actin (α—SMA)	ACTGGTATTGTGCTGGACTCTG	TAGTCACGAAGGAATAGCCACG
Smooth muscle (SM22α)	CCCAGACACCGAAGCTACTC	GACTGCACTTCTCGGCTCAT
h-caldesmon	TACACCAATGCAATCGAGGGAA	TACATCTCCTGGCCTCAAGTCA